



**HAL**  
open science

## Turbulence Over Camarinal Sill and Its Impact on Water Mixing-Strait of Gibraltar

Jean-Baptiste Roustan, Pascale Bouruet-Aubertot, Lucie Bordoï, Yannis Cuypers, Xavier Carton, Franck Dumas, Francis Auclair

► **To cite this version:**

Jean-Baptiste Roustan, Pascale Bouruet-Aubertot, Lucie Bordoï, Yannis Cuypers, Xavier Carton, et al.. Turbulence Over Camarinal Sill and Its Impact on Water Mixing-Strait of Gibraltar. Journal of Geophysical Research. Oceans, 2024, 129 (6), 10.1029/2023jc020709 . hal-04650354

**HAL Id: hal-04650354**

**<https://hal.science/hal-04650354v1>**

Submitted on 17 Jul 2024

**HAL** is a multi-disciplinary open access archive for the deposit and dissemination of scientific research documents, whether they are published or not. The documents may come from teaching and research institutions in France or abroad, or from public or private research centers.

L'archive ouverte pluridisciplinaire **HAL**, est destinée au dépôt et à la diffusion de documents scientifiques de niveau recherche, publiés ou non, émanant des établissements d'enseignement et de recherche français ou étrangers, des laboratoires publics ou privés.



Distributed under a Creative Commons Attribution - NonCommercial - NoDerivatives 4.0 International License

## Turbulence Over Camarinal Sill and Its Impact on Water Mixing—Strait of Gibraltar

**Key Points:**

- Dissipation rates of TKE are inferred near the Camarinal Sill with maximum values of  $10^{-3}$  W/kg in the hydraulic jump
- The spatio-temporal distribution of dissipation rates near Camarinal Sill shows maxima on the western flank in tidal outflows
- Mixing rates are similar during spring and neap tides except for the Atlantic waters more impacted by spring tide hydraulic jumps

**Correspondence to:**

J.-B. Roustan,  
[jean-baptiste.roustan@polytechnique.edu](mailto:jean-baptiste.roustan@polytechnique.edu)



**Citation:**

Roustan, J.-B., Bouruet-Aubertot, P., Bordoio, L., Cuypers, Y., Carton, X., Dumas, F., & Auclair, F. (2024). Turbulence over Camarinal Sill and its impact on water mixing—Strait of Gibraltar. *Journal of Geophysical Research: Oceans*, 129, e2023JC020709. <https://doi.org/10.1029/2023JC020709>

Received 13 NOV 2023  
 Accepted 21 MAY 2024

**Author Contributions:**

**Conceptualization:** Jean-Baptiste Roustan, Lucie Bordoio  
**Data curation:** Jean-Baptiste Roustan  
**Funding acquisition:** Lucie Bordoio, Franck Dumas  
**Methodology:** Jean-Baptiste Roustan, Pascale Bouruet-Aubertot, Yannis Cuypers  
**Project administration:** Lucie Bordoio, Franck Dumas  
**Software:** Jean-Baptiste Roustan, Pascale Bouruet-Aubertot, Yannis Cuypers  
**Supervision:** Pascale Bouruet-Aubertot, Lucie Bordoio, Xavier Carton, Franck Dumas, Francis Auclair  
**Writing – original draft:** Jean-Baptiste Roustan

Jean-Baptiste Roustan<sup>1,2</sup> , Pascale Bouruet-Aubertot<sup>3</sup>, Lucie Bordoio<sup>4</sup>, Yannis Cuypers<sup>3</sup>, Xavier Carton<sup>1</sup>, Franck Dumas<sup>4</sup>, and Francis Auclair<sup>5</sup> 

<sup>1</sup>University Brest, CNRS, Ifremer, IRD, Laboratoire d'Océanographie Physique et Spatiale (LOPS), IUEM, Plouzané, France, <sup>2</sup>Direction Générale de l'Armement, Ministère des Armées, Paris, France, <sup>3</sup>Laboratoire d'Océanographie et de Climatologie par Expérimentation et Approche Numérique (LOCEAN), Sorbonne Université, Paris, France, <sup>4</sup>Service Hydrographique et Océanographique de la Marine (SHOM), Brest, France, <sup>5</sup>Laboratoire d'Aérodynamique (LA), Toulouse, France

**Abstract** Straits and narrows are the place of intensified turbulent mixing. Deep understanding of the turbulent dynamics at these locations is of crucial importance as it conditions the properties of the water masses flowing in the open ocean. A new extensive field experiment, PROTEVS GIB20, with high frequency measurements has been conducted in the Strait of Gibraltar. It allows us to infer dissipation rates of the turbulent kinetic energy,  $\epsilon$ , from two consistent methods. The range of  $\epsilon$  is depicted for the different processes which developed in the vicinity of Camarinal Sill, the main topographic feature of the Strait of Gibraltar. It evidences that the bottom boundary layer, hydraulic jumps and large overturns are the main loci of intensified turbulence reaching  $10^{-3}$  W.kg<sup>-1</sup>. The variability of the turbulence is mainly controlled by semi-diurnal, diurnal and fortnightly tidal oscillations. Spatially, the western flank of Camarinal Sill is evidenced as the hotspot for turbulent mixing. We confirm a weak variation of the spatially averaged vertically integrated turbulent dissipation rate. This result needs to be qualified in view of the differentiated impact of the various processes on adjacent water masses. The dynamics of the spring tide directly mix Atlantic and Mediterranean waters, resulting in a large spreading of the T-S diagram.

**Plain Language Summary** A recent field experiment, PROTEVS GIB20, was performed in the Strait of Gibraltar in October 2020. This experiment was partly designed to observe the turbulent dynamics of the flow in this region. The Strait of Gibraltar presents an important topographic sill, Camarinal Sill, where the current reaches its maximum value enhancing the turbulent processes. Quantifying the turbulence intensity and the associated mixing that develops there is of crucial importance to understand the impact of small-scale process on larger/regional scales which is now recognized but remains incompletely understood. Such measurements are necessary to assess the performances of the parametrization use in climate model which to dot represent such small-scale dynamics. Direct measurements of dissipation rate of turbulent kinetic energy are rare near Camarinal Sill, due to the rough environment and strong maritime traffic. From different methods, we infer time series and spatial averages of the turbulence dissipation rate. We describe the variability of the turbulence, the physical processes involved and the impact on water mass mixing.

### 1. Introduction

Straits, narrows and topographic constrictions are of great importance for the ocean circulation as they connect different basins. Thus their local dynamics control inflowing and outflowing water masses at regional scale. These places are influenced by complex bathymetry, which leads to dynamical interactions between topography and water flow. This interaction results in vigorous mixing, potentially amplified by additional factors like tidal activity. Abyssal constrictions drive modification of the water masses in deep overflows affecting the large scale meridional overturning. Turbulent dissipation rates,  $\epsilon$ , of  $10^{-8}$  W.kg<sup>-1</sup> were measured in the Samoan passage where the Antarctic water flows in north Pacific Ocean (Carter et al., 2019; Cusack et al., 2019). Fjords connect the shelf waters with the fresh runoff inputs. Turbulent dissipation rates of  $10^{-4}$  W.kg<sup>-1</sup> were measured in Knight Inlet (British Columbia) (Klymak & Gregg, 2004) and  $10^{-3}$  W.kg<sup>-1</sup> in the Oslofjord sill (Norway) (Staalstrom et al., 2015). Straits directly connect different basins at a regional scale. The turbulent dissipation rate measured in these places strongly varies with for examples  $\epsilon$  of  $10^{-2}$  W.kg<sup>-1</sup> in the Strait of Gibraltar (Wesson & Gregg, 1994),  $10^{-5}$  W.kg<sup>-1</sup> in the Lombok and Ombai Straits (Bouruet-Aubertot et al., 2018; Purwandana et al., 2021) and

© 2024. The Author(s).

This is an open access article under the terms of the [Creative Commons Attribution-NonCommercial-NoDerivs License](https://creativecommons.org/licenses/by/4.0/), which permits use and distribution in any medium, provided the original work is properly cited, the use is non-commercial and no modifications or adaptations are made.

Writing – review & editing:

Pascale Bouruet-Aubertot, Lucie Bordois,  
Yannis Cuyppers, Xavier Carton,  
Francis Auclair

$10^{-6} \text{W.kg}^{-1}$  in the Sicily channel (Vladoiu et al., 2018). In any cases,  $\epsilon$  in these places is orders of magnitude higher than the dissipation rates measured in the ocean interior far from the boundary layers, which is about  $10^{-10} \text{W.kg}^{-1}$  in the Mediterranean Sea (Ferron et al., 2017).

The Strait of Gibraltar (SoG hereafter) gathers in a single place intense overflow, strong tide and complex bathymetry, with a main topographic feature, Camarinal Sill (CS hereafter). An inverse estuarine circulation is driven by the density difference between Atlantic waters and Mediterranean waters (Bryden et al., 1994; Jorda et al., 2017; Lacombe & Richez, 1982). Therefore, a continuous baroclinic circulation takes place in the SoG with the Atlantic jet flowing eastward over the Mediterranean outflow which flows westward. This circulation is modulated at different time-scales by intense tidal currents (Candela et al., 1990; Lafuente et al., 1990, 2000), atmospheric-forced sub-inertial flow (Candela et al., 1989; Lafuente et al., 2002) and long-term changes of the water masses characteristics (García-Lafuente et al., 2021; Naranjo et al., 2017).

The hydrographical properties of the Mediterranean water are of crucial importance for the large scale interaction, both in the Gulf of Cadiz and in the Atlantic Ocean. In the Gulf of Cadiz, the density of the Mediterranean outflow directly impacts its equilibrium depth and thus the depth at which Meddies form and detach from the continental slope (Papadakis et al., 2003). At the eastern end of the SoG, the T-S properties of the Atlantic waters entering the Mediterranean basin impact the circulation of the Mediterranean Sea, including the formation of the Deep Mediterranean Waters in the Gulf of Lions (Sannino et al., 2015). Therefore, a precise understanding of the mixing in the SoG is of crucial importance as it conditions large scale circulation.

Different high-frequency processes have been described in the vicinity of CS: internal tides, internal hydraulic jumps, shear-instabilities at the top of a thick bottom boundary layer (Armi & Farmer, 1988; Hilt et al., 2020; Roustan et al., 2023; Sanchez-Garrido et al., 2011; Wesson & Gregg, 1994). All these events lead to intense turbulent mixing at CS, which modifies the Mediterranean and Atlantic waters during their advection in the SoG. East of the SoG, different Mediterranean waters are present: dense West Mediterranean Deep Water (WMDW) near the southern boundary and lighter Levantine Intermediate Waters (LIW) along the Spanish coast (Millot, 2009; Naranjo et al., 2015). The westward flow of Mediterranean Water starts eroding at CS and its mixing is particularly noticeable at Espartel Sill (Lafuente et al., 2011). Note that the Mediterranean Water outflow properties are a subject of intense debate (Millot, 2014, 2017; Naranjo et al., 2015).

Recently, Gonzalez et al. (2023) analyzed the impact of tides on mixing in the SoG using a 1 km resolution, hydrostatic model of the SoG. They showed that tide-induced turbulence was favored by the weakening of the stratification and by the intensification of the shear. The former mechanism is active during tidal outflows (westward-heading tidal currents), when the Mediterranean Water is upwelled over the sill. This partly destroys the stratification and facilitates the development of shear instabilities. The latter mechanism is the main source of turbulent mixing during the whole tidal cycle, in particular near the bottom. Macias et al. (2006) analyzed the tidal variability of the mixing processes based on water mass diagnostics. They observed different water masses at the different stages of the tidal cycle. The volume of North Atlantic Central Water (NACW), in a thin layer near the main pycnocline, is inversely proportional to the tidal outflow strength; this illustrates the impact of the tide on the mixing processes. Lafuente et al. (2013) analyzed the mixing dynamics with a high resolution non-hydrostatic model of the SoG (Sanchez-Garrido et al., 2011). They illustrated the fortnightly variations in thickness of the interfacial layer; it is thicker in spring tides and it shows larger oscillations. These authors proposed three mechanisms to account for these thickness oscillations: horizontal advection, water entrainment and internal wave mixing. The advection convey the interfacial water mainly formed on the lee side of CS. The entrainment erodes the salinity gradient increasing the thickness of the layer while internal waves favor shear instabilities in the interior of the interfacial layer.

In-situ measurements of turbulence in the SoG are rare. They consist essentially in two sets of micro-structure measurements, one during neap tide and a shorter one during spring tide, achieved during the *Gibraltar Experiment* (Kinder & Bryden, 1987). From this data set, Wesson and Gregg (1994) computed turbulent dissipation rate reaching  $10^{-2} \text{W.kg}^{-1}$  in  $O(75 \text{ m})$  tall structures, west of CS, in neap tide outflows. These data also showed a high variability of the turbulent energy dissipation. Sections 1 km apart could present orders of magnitude differences in  $\epsilon$  even at the same tidal phase. Such differences were due to the rugged topography near CS and to the high-frequency processes which generated bursts of turbulence. In neap tide outflows, the study mentioned above showed that the interfacial waters were the most affected by mixing. During inflows, the turbulence was enhanced at the front between arrested Mediterranean waters and Atlantic waters flowing eastward.

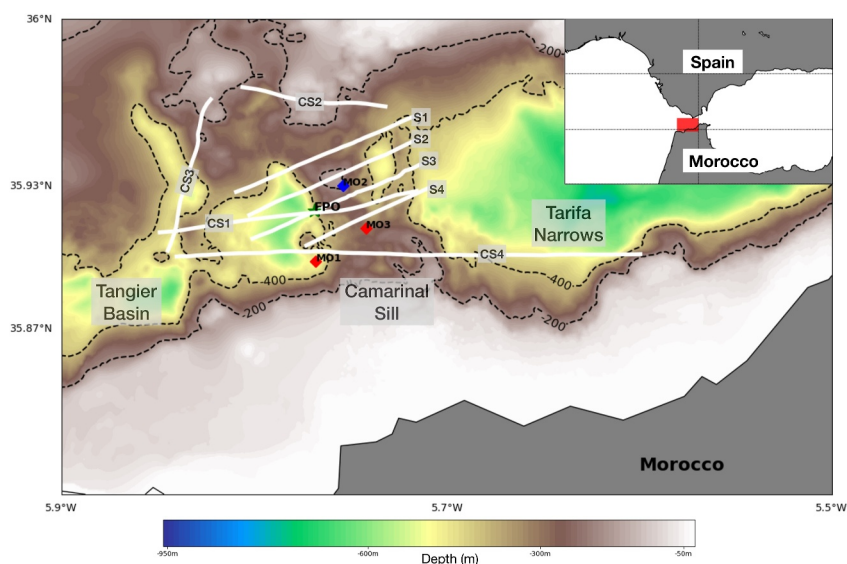


**Figure 1.** Inset: Map of the PROTEVS GIB20 measurements. The red box is the area analyzed in this paper. **Map:** Bathymetry of the Camarinal Sill region superimposed with the position of the hydrographical moorings MO1, MO3 (red diamonds) and the current profiler MO2 (blue diamond). The sections S1, S2, S3, S4, CS1, CS2, CS3, and CS4 are depicted with white lines. The average position of FPO station is shown with a green star.

In spring tide, these authors found a similar order of magnitude for the averaged dissipation rates but their measurements were quite sparse. Furthermore, the deepest part of the water column, typically below 250 m depth, was not sampled during this experiment. At the western ends of the SoG—Spartel West Sill, 50 km west of CS—Nash et al. (2012) inferred turbulent rate of about  $10^{-5} \text{ W.kg}^{-1}$  within the Mediterranean vein. The authors evidenced this place as possible hotspot for mixing along the Mediterranean outflow pathway.

A new in-situ data set, obtained during the PROTEVS GIB 2020 experiment, provides complementary information on the dissipation rates near CS. This experiment was designed to study the tide-varying dynamics over a fortnightly cycle (Roustan et al., 2023). Different measurements allow us to calculate turbulent dissipation rates from a few meters above the sea floor, up to a few tens of meters below the surface. High-frequency moorings give access to time series of the turbulent dissipation rates. The analysis of turbulent dissipation of the Atlantic inflow and Mediterranean outflow in this data set is the subject of the present paper.

Sections 2 and 3 present the PROTEVS GIB 2020 data -set and the methods used to infer the dissipation rate of turbulent kinetic energy,  $\epsilon$ . Then, this paper addresses three main questions. Section 4 compares the levels of turbulence associated with different processes described by Roustan et al. (2023) during this field experiment. Section 5 addresses the space-time variability of the turbulent dissipation rate during a fortnightly cycle. Finally, Section 6 quantifies the impact of the turbulent dynamics on the water masses encountered in the SoG. We provide details on the different intensity of mixing between the spring tides and neap tides. In the final section, we discuss the results and we draw conclusions.

## 2. Data

The PROTEVS GIB20 experiment was an intensive survey in the SoG, the Bay of Cadiz and the Alboran Sea during a fortnightly cycle in October 2020. The data set analyzed in this paper is described by Roustan et al. (2023). We remind its main features. This experiment was designed to measure the turbulent structures near CS. The turbulence estimates are inferred here from fine-scale current and hydrographical measurements (see methodology in Section 3). Free-fall micro-structure soundings were not performed due to strong currents and to an intense maritime traffic.

Three moorings sampled hydrographical (MO1, MO3) and current (MO2) variables, at very high frequency in the whole water column, around CS. Sections were performed during both spring and neap tides. The location of the measurements is summarized in Figure 1. Acoustic back-scatters (via SIMRAD EK60 echo-sounder at 38 kHz)

**Table 1**  
*Description of the Sections*

Sections	Instruments	Time laps (UTC)	Tide phase	Tidal current direction
Spring tides				
S4_1ST	MVP + EK60 + S-ADCP	2020/10/17 17:26–2020/10/17 18:04	LW-2	Inflow (eastward)
S1_1ST	MVP + EK60 + S-ADCP	2020/10/17 19:04–2020/10/17 20:37	LW	Flow inversion
S3_ST	MVP + EK60 + S-ADCP	2020/10/17 21:02–2020/10/17 23:02	LW+2	Outflow (westward)
S2_ST	MVP + EK60 + S-ADCP	2020/10/17 23:18–2020/10/18 00:04	LW+4	Outflow (westward)
S4_2ST	MVP + EK60 + S-ADCP	2020/10/18 00:27–2020/10/17 02:35	LW+5	Outflow (westward)
CS1	MVP + EK60 + S-ADCP	2020/10/17 11:02–2020/10/17 13:50	LW+3/6	Outflow (Westward)
CS2	MVP + EK60 + S-ADCP	2020/10/19 11:34–2020/10/19 12:04	LW+2	Outflow (Westward)
CS3	MVP + EK60 + S-ADCP	2020/10/19 12:12–2020/10/19 13:18	LW+3	Outflow (Westward)
CS4	MVP + EK60 + S-ADCP	2020/10/19 13:26–2020/10/19 16:42	LW+4/6	Outflow (Westward)
Neap tides				
S4_NT	MVP + EK60 + S-ADCP	2020/10/10 15:15–2020/10/10 16:38	LW+2	Outflow (Westward)
S2_NT	MVP + EK60 + S-ADCP	2020/10/10 16:54–2020/10/10 18:05	LW+4	Outflow (Westward)
S3_NT	MVP + EK60 + S-ADCP	2020/10/10 18:23–2020/10/10 19:35	LW+5	Outflow (Westward)

*Note.* LW is for Low Water at Tarifa tide gauge.

and velocity measurements (via Ship-mounted Acoustic Doppler Current Profile (S-ADCP) RDI OS 38 kHz) were recorded on-board. The S-ADCP sampled at 1 Hz, the current is averaged in 1 min frame and 8 m width bins.

The hydrographical mooring lines MO1 and MO3 were equipped with SBE37 and SBE56 sensors (see Table 1 of Roustan et al. (2023) for details). SBE37 are temperature, conductivity and pressure pumped probes sampling at 10 s; SBE56 sensors measure only temperature at 1 s. They were deployed along a mooring line from the bottom to about 50 m below the surface. The pressure gauges were essential because currents could tilt the mooring line during spring tide. The depth of the SBE56 was assessed from the pressure measurement of the nearest SBE37 under the assumption of a rectilinear mooring line between SBE37. SBE56 are distant by 10 m from each other and they are interspersed between two SBE37, themselves distant by 50 m on average. The Conductivity Temperature data were then interpolated at fixed depths. Due to the mooring line tilting, no data was recorded in the Atlantic layer during the strongest tides especially at MO1 and MO3. MO2 mooring was equipped with a four beams CONTINENTAL 190 kHz Acoustic Doppler Current Profiler (ADCP) pointing upward. The beam makes a 18° angle with the vertical. It was deployed from the eighth of October to the seventeenth of October (see Table 1 of Roustan et al. (2023) for details). This instrument sampled the currents in the water column from the bottom up to 37 m below the surface at 30 s intervals (30 measures per interval) with vertical bins of 5 m.

Hydrographical sections, about 10 km long, were performed perpendicularly to the isobaths during both neap and spring tides. Four sections named S1, S2, S3 and S4 from North to South (Figure 1) were performed at least once during neap tide (on the tenth of October) and once during spring tide (between the seventeenth and the eighteenth of October) (Table 1). Along the sections, a moving vessel profiler (MVP) equipped with CTD probes was towed at around 4 knots. The sections called CS1, CS2, CS3, CS4 were performed once, around the sill, to complement this data set (Figure 1 and Table 1).

In addition, we present the results of a 5-hr station performed on the western slope of CS during a tidal outflow on the eleventh of October afternoon (FPO in Figure 1). Three CTD casts were performed during this station. Note that the CTD cage was equipped with two pairs of C-T probes, one at the top and the second at the bottom to allow reliable measurements in both ascending and descending phases, minimizing errors due to water entrainment.

### 3. Methodology

Two different methods are used here to calculate the dissipation rate of turbulent kinetic energy,  $\epsilon$ , with the different sensors deployed during GIB20. Indirect computations are applied to CTD profiles and MVP casts on

the one hand and to high frequency temperature mooring data on the other hand. The inter-comparison of the methods shows good agreement illustrating the reliability of the methods (see Section 7).

### 3.1. Thorpe Length Method Applied to CTD-MVP Casts

The second method is based on the classical Thorpe length  $L_T$  (Thorpe & Deacon, 1977) which measures the length scales of the turbulent vortices. The Thorpe length is the root-mean-squared Thorpe displacement in turbulent patches; this definition holds for sections where the Thorpe displacements sum up to zero vertically. The Thorpe displacements measure the vertical distance between a point in the density profile and its position in the stably ordered equivalent profile (see Thorpe and Deacon (1977) for details). In a stratified environment, the size of the primary structures of the turbulent cascade is restricted by the Ozmidov length  $L_O$  (Equation 1), with  $\epsilon$  the turbulent dissipation rate and  $N$  the Brunt-Väisälä frequency.

$$L_O = \sqrt{\epsilon N^{-3}} \quad (1)$$

Dillon (1982) showed that the Thorpe length is proportional to the Ozmidov length with a coefficient related to the ratio of the gradient and flux Richardson numbers. This author noticed that, except near the surface, the coefficient remains fairly constant. Unfortunately, we cannot estimate its value from micro-structure measurements, which were not performed during our experiment; therefore, we take  $L_O = 0.8L_T$  as done in previous studies (Ferron et al., 1998; Moum, 1996; Purwandana et al., 2021) including in the vicinity of the SoG (Nash et al., 2012). Wesson and Gregg (1994) found with their micro-structure measurements  $0.25L_T \leq L_O \leq 4L_T$ , a range including the 0.8 chosen here. Thus, we estimate  $\epsilon_T$  from Equation 2. Note that the buoyancy frequency,  $N$ , is computed from the ordered (stable) density profile averaged in the turbulent patches in such a way that we provide one value of  $\epsilon_T$  per patch.

$$\epsilon_T = 0.64 L_T^2 N^3 \quad (2)$$

This method requires a careful detection of the overturns in the density profiles. The main systematic error is a spurious detection of overturns due to noise. To solve this issue, we estimated a noise level of our instrument from the standard deviation of density in a depth interval with a weak density gradient. This provided a noise level of  $10^{-3} \text{ kg m}^{-3}$ ; finally, we took  $2.10^{-3} \text{ kg m}^{-3}$  for both CTD-MVP profiles to ensure the elimination of spurious noisy overturns. This choice is conservative compared to other studies, which retained  $5.10^{-4} \text{ kg m}^{-3}$  (Gargett & Garner, 2008). Then we applied the algorithm described by Ferron et al. (1998) and modified by Gargett and Garner (2008) to eliminate those spurious overturns. Gargett and Garner (2008) proposed a second quality check based on the symmetry of the overturns, that we implemented.

Finally, we checked carefully the possible thermal lag on the conductivity probes to avoid spurious overturns at the thermocline. First, we looked at each profile to tag the spikes. Then, we performed a wavelet decomposition of the C-T profiles in wavelengths to ensure that conductivity variations were not offset from those in temperature. This analysis showed no offset between C and T for both CTD and MVP profiles.

### 3.2. Ellison Length Method Applied to Moored High Frequency Temperature Sensors

During the GIB20 experiments, we deployed 2 moorings MO1 and MO3 with high frequency SBE56 temperature probes (see Section 2) in the deeper part of the water column. With the temperature field during the whole deployment of the moorings, we calculated the dissipation rates based on the Ellison scale. This scale is the ratio between temperature fluctuations and its vertical mean gradient (Moum, 1996). The Ellison scale  $L_E$  is computed from Equation 3:

$$L_E = \frac{\sqrt{\overline{\theta'^2}}}{d\bar{\theta}/dz} \quad (3)$$

with  $\theta'$  the fluctuations of the potential temperature and  $\bar{\theta}$  the time average of potential temperature (Cimatoribus et al., 2014).

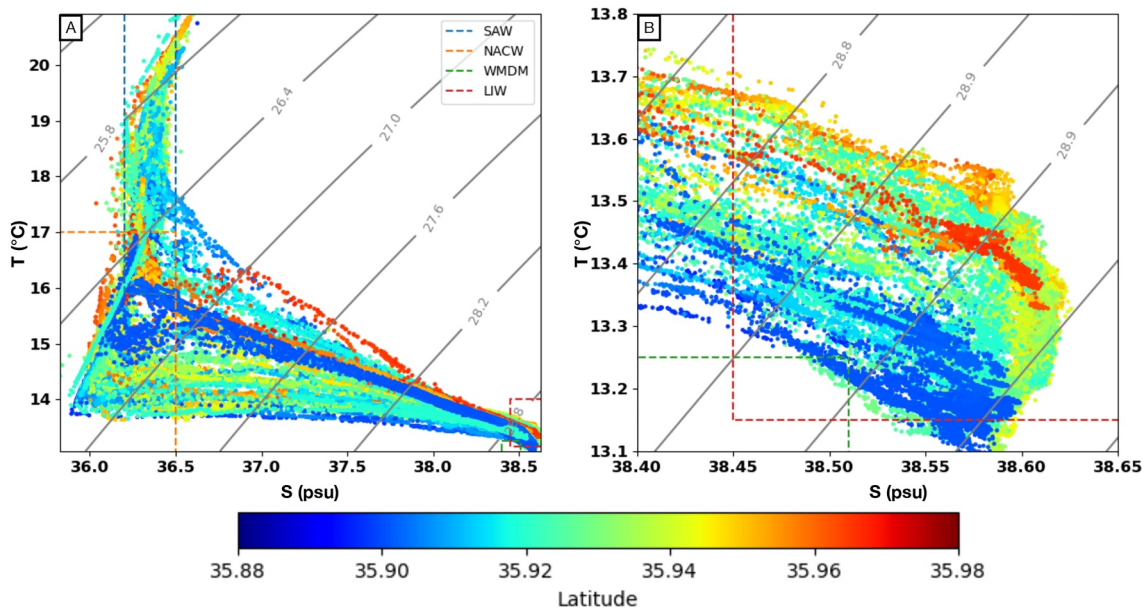


**Figure 2.** (a) T-S diagram of the CTD-MVP profiles. Isopycnals are depicted in gray. Colored dashed lines define the principal water masses (see text for details). (b) zoom of (a) on the Mediterranean waters.

As the SBE56 measure only temperature, we could not compute fluctuations of potential temperature. Thus, in our  $L_E$  computation,  $\theta'$  is in-situ temperature. This should not alter the results because fluctuations are calculated around a mean value for a short time (less than 1 hour). Conversely, the low frequency vertical gradient,  $d\theta/dz$ , was computed from the 10 s potential temperature fields provided by pumped CTD SBE37 sensors. Note that the salinity data have been interpolated on a 10 m spaced fixed grid.

From the Ellison scale  $L_E$ , we derive the turbulent dissipation rate  $\epsilon_E = L_E^2 N^3$ , where  $N$  is the Brunt-Väisälä frequency (Cimatoribus et al., 2014; Purwandana et al., 2021).

For the calculation of  $L_E$ , three parameters need to be set: the lowest frequency of the high frequency band, the lapse for the temporal mean and finally the scale for the temperature gradient computation. First, as the SoG, and CS especially, are known to support high frequency internal solitary waves, we chose a high cutoff frequency of 1/60 Hz applied with a eighth order Butterworth filter to compute the temperature fluctuations. Such a filter had previously been used in the study of Purwandana et al. (2021) in the Lombok Strait. This strait has comparable dynamics to the SoG; in particular, the buoyancy is similar:  $N^2 \approx 10^{-4} s^{-2}$  in the two straits. The frequency spectrum of temperature at MO1 at 400 m depth indicates that the inertial-convective sub-range starts at 10cph, or 1/360 Hz (not shown). Thus, we averaged with 2 min sliding windows. Finally we computed the gradient with the nearest sensors at  $\pm 10$  m from the depth of interest. We made sensitivity tests to support our choices that are presented in Appendix A. The surface waves are not an issue for our computation as the temperature sensors are deep compared to the surface wavelength.

Finally, note that the Ellison method based on temperature fluctuations holds as long as temperature inversions marks density inversions. The Ellison method is applied here in the deepest part of the water column. This avoids data gaps due to the tilting of the mooring. The careful inspection of the T-S diagram, provided in Figure 2—based on the CTD measurement performed in the vicinity of CS - shows that the T-S diagram is piecewise linear. Therefore any temperature fluctuations signs for density fluctuations except near the elbow point of the T-S diagram where some density fluctuation might not have any temperature signature, possibly underestimating the turbulence there.

### 3.3. Water Masses in the Area

Part of this study aims at characterizing the impact of turbulent mixing on water mass properties. Figure 2 shows a T-S diagram of the water masses sampled in the vicinity of CS during the field experiment. The water masses are

**Table 2**  
*Description of the Water Masses Encountered in the SoG*

Water masses	Temperature limits (°C)	Salinity limits (psu)
South Atlantic Water (SAW)	$15.9 \leq T \leq 22.7$	$36.2 \leq S \leq 36.5$
North Atlantic Central Water (NACW)	$11 \leq T \leq 17$	$35.2 \leq S \leq 36.5$
Levantine Intermediate Waters (LIW)	$13.15 \leq T \leq 14$	$38.45 \leq S \leq 38.75$
West Mediterranean Deep Water (WMDW)	$12.7 \leq T \leq 13.25$	$38.4 \leq S \leq 38.51$
Tyrrhenian Deep Waters (TDW)	$12.8 \leq T \leq 13.1$	$38.44 \leq S \leq 38.58$
Winter Intermediate Waters (WIW)	$12.5 \leq T \leq 13.8$	$37.9 \leq S \leq 38.3$

*Note.* T-S limits are retained from a review of (Naranjo et al., 2015).

defined via minimum and maximum T-S values described in the literature (Table 2 in Naranjo et al. (2015)). The ranges of T and S retained here, are presented in Table 2. The main water masses encountered in the SoG are the South Atlantic Waters (SAW) and the NACW from the Atlantic side and the LIW from the Mediterranean basin. The other typical Mediterranean waters are: the WMDW, the Tyrrhenian Deep Waters and the Winter Intermediate Waters (WIW). They are not considered in this study for different reasons. The first two water masses are not observed in our CTD-MVP profiles (see Figure 2b). The MVP soundings do not exceed 400 m depth, and our sections were performed over or west of CS (except for CS4) where those waters masses are not present, according to Naranjo et al. (2015). The WIW is not considered as its T-S signature is along the mixing line between the LIW and the NACW. Therefore, without other information it is not distinguishable from mixed water. We admit that our water mass definition is crude and presents overlaps between NACW and SAW, but it is sufficient to support our discussion of the mixing dynamics near CS.

### 3.4. Diapycnal Diffusivity Computation

To better understand the mixing associated with the turbulent dissipation rate, we computed (when density measurements were available) the diapycnal diffusivity  $\kappa_z$ . We used the recent parameterization of Bouffard and Boegman (2013), which complements the traditional Osborn (1980) relation. First, the turbulence intensity  $I$  is defined by Equation 4, with  $\epsilon$  the turbulent dissipation rate,  $N^2$  the squared Brunt-Väisälä frequency and  $\nu$  the molecular viscosity:

$$I = \frac{\epsilon}{\nu N^2} \quad (4)$$

This ratio quantifies the destabilizing effect due to turbulence versus stabilizing processes: viscosity and stratification. Then, the Bouffard and Boegman (2013) formulation of  $\kappa_z$  defines four regimes based on  $I$ :

- The diffusive sub regime for  $I < 1.7$ :  $\kappa_z = 10^{-7} (m^2/s)$
- The buoyancy controlled sub-regime for  $1.7 \leq I \leq 8.5$ :  $\kappa_z = \frac{0.1}{7^{1/4}} \nu I^{3/2} (m^2/s)$
- The intermediate regime for  $8.5 \leq I \leq 400$ , with classical Osborn (1980) formulation:  $\kappa_z = 0.2 \nu I (m^2/s)$
- The energetic regime for  $I > 400$ :  $\kappa_z = 4 \nu I^{1/2} (m^2/s)$

## 4. Dissipation Rates and Turbulent Processes Near Camarinal Sill

The neap/spring inflow/outflow dynamics in the vicinity of CS during PROTEVS GIB20 field experiment is widely described in Roustan et al. (2023). The authors described the hydraulic of the flow from the composite Froude number model:  $G^2 = F_1^2 + F_2^2$  with  $F_i^2$  the Froude number of layer  $i$  defined as  $F_i^2 = \frac{U_i^2}{g' H_i}$  with  $g' = g \frac{\Delta \rho}{\rho_0}$  the reduced gravity,  $g$  the gravitational acceleration,  $\rho_0$  the density reference and  $\Delta \rho$  the density difference between the two layers.

Different turbulent processes were identified near CS depending on the location and strength of tidal current which varies from  $-0.5$  m/s to  $-2$  m/s at the peak of tidal outflow (flood phase) from neap to spring tides during the field experiment. During neap tide outflows, the flow remained locally subcritical ( $G^2 < 1$ ) over CS, with the Mediterranean outflow acting like a tidally modified gravity current. Along the interface between Mediterranean



and Atlantic waters shear instabilities developed, and a bottom boundary layer was observed. In intermediate tides, the Mediterranean vein detached from the slope, generating tall vortices of 200 m height on the west flank of CS. In spring tide outflows, hydraulic control happened over CS ( $G^2 > 1$ ) and large hydraulic jumps formed at the transition from supercritical to subcritical flow. A high frequency variability of the baroclinic current was observed over the main sill at MO2 when the flow became supercritical over CS. Note that, The baroclinic current is defined as the total current  $U$  minus the vertically averaged  $\bar{U}$  at MO2. This variability was a priori related to the wake of a hydraulic jump located upstream of the main sill.

The present section describes the turbulence associated with these processes and discusses its implication on mixing dynamics. First, we describe the spring/neap tide dynamics over the sill at MO2 and MO3. Then we characterize the turbulence in the Mediterranean outflow on the lee side of CS. Finally, we evaluate the turbulence near the hydraulic jumps during spring tides.

#### 4.1. Turbulence Over Camarinal Sill

The dynamics over CS mainly depends on the tidal forcing modulated by the low frequency baroclinic exchange flow. During the PROTEVS GIB 20 experiment, the structure of the baroclinic zonal current exhibited strong changes during spring tides with the two-layer structure of the density-driven flow strongly modified during the tidal outflow phase (Roustan et al., 2023). During this time period (21:00-00:00 the fifteenth and from 09:00 the sixteenth) high-frequency variations of the baroclinic current occurred (Figure 3a). Conversely, the two-layer flow was less influenced by the tidal phase during neap tides, with only a moderate influence of the diurnal tide (Figure 3c). Finally, the 30 m thick bottom layer displayed oscillations of the vertical velocities over a few minutes (not shown). Such overturns are typical of bottom turbulence enhanced by the rough topography of the sill and by the accelerating Mediterranean waters in tidal outflows. In the following, we calculate  $\epsilon$  during both neap and spring tides at MO3 with the Elisson Method (respectively Figures 3b and 3d).

##### 4.1.1. Spring Tide Dynamics

During spring tide, a key feature is the contrast between the tidal inflow/outflow dynamics, the latter being more turbulent than the former. The hydraulic control over CS that happens during outflow reduces the stratification and favors the development of shear instabilities.

During the tidal inflow, at MO3, the dissipation rates vary from  $10^{-6}$  to  $10^{-4} \text{W.kg}^{-1}$  with some intense bursts. The lowest turbulence occurred in the pycnocline (14:00 to 17:00 and 03:00 to 06:00 between the two depicted isopycnals Figure 3b). The stratification stabilizes the flow in the vicinity of the pycnocline preventing the development of shear instabilities within the pycnocline, but shear instability generating fairly intense dissipation rates develops within the Mediterranean and Atlantic layer where stratification is weaker.

During the spring tide outflow,  $\epsilon$  varied widely with the dynamics developed at CS. From 19:00 to 20:00, an intense shear layer marked the interface between the density driven flows (Figure 3a). Simultaneously, the dissipation rates increased in the interfacial mixed layer at MO3, approaching  $10^{-3} \text{W.kg}^{-1}$ .

The two-layer baroclinic flow vanished during the 4 hours of the maximal westward tidal current that is, during the transition from subcritical to supercritical flow at MO2 (Roustan et al., 2023). At this stage, the dissipation rate in the water column fluctuated around  $10^{-4} \text{W.kg}^{-1}$  at MO3 with intense bursts. In supercritical flow, the shear layers were thinner and patchy except near in the BBL, but the stratification was also weaker, as indicated by the spacing of the isopycnals. Therefore, in this weakly stratified environment, shear instabilities could trigger the turbulent bursts.

The two-layer baroclinic flow was recovered at 00 : 45 when the tidal current slackened and the flow returns subcritical (Roustan et al., 2023) accompanied by a noticeable decrease of the turbulence except in the near the bottom. The rapid plunge of the shallowest isopycnal (at 00:50 in Figure 3b) depicts a westward propagating bore which precedes a softly turbulent period near the upper interface.

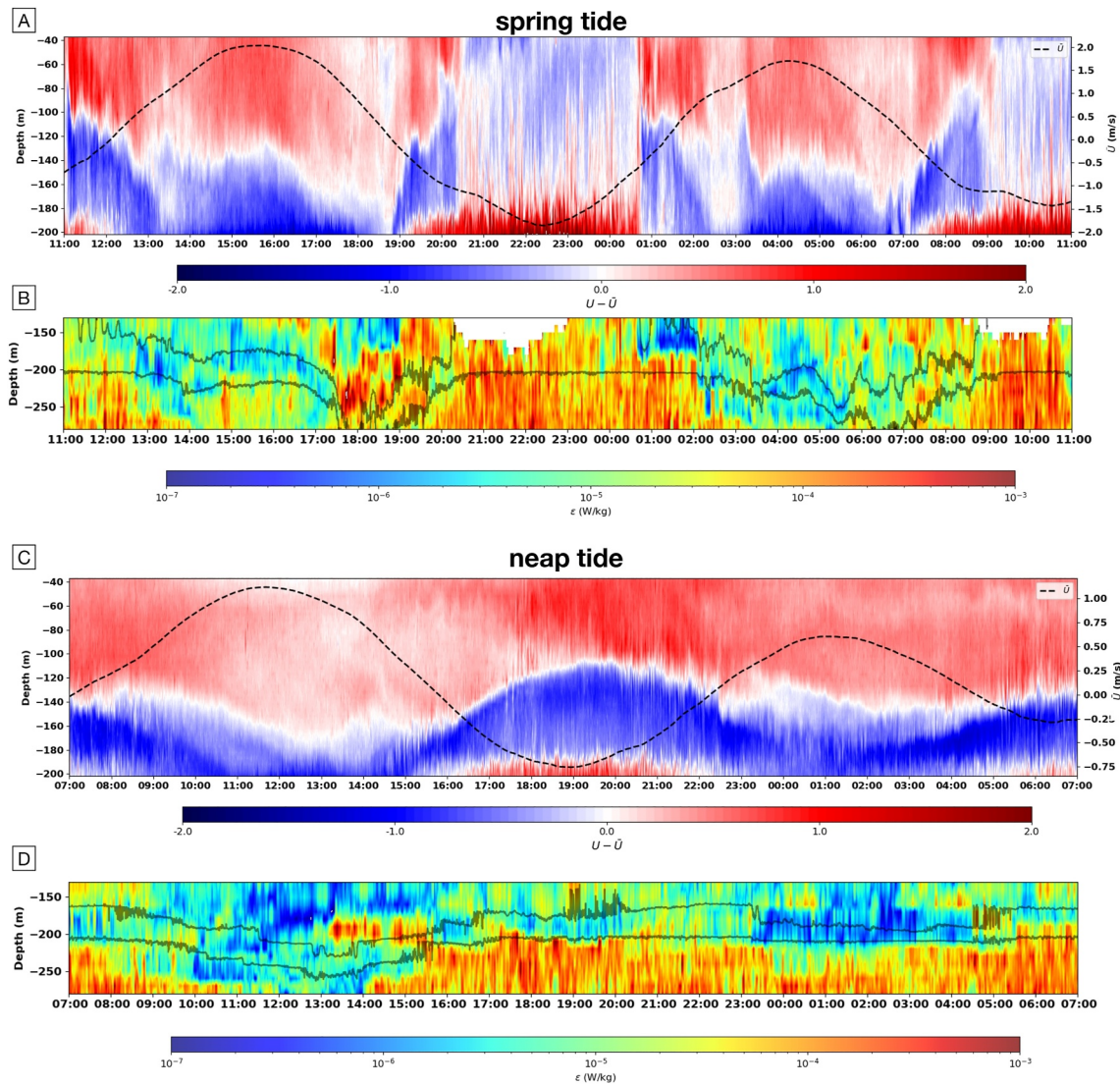


**Figure 3.** (a) Zonal baroclinic current with zonal barotropic current superimposed (black dashed curve right axis) at MO2, (b)  $\epsilon_E$  at MO3 superimposed with isopycnals 1028 and 1029  $\text{kg}\cdot\text{m}^{-3}$  (from 11:00 on the fifteenth of October to 11:00 on the sixteenth of October). (c) and (d) are equivalent for two neap tide cycles (from 07:00 on the eleventh of October to 07:00 on the twelfth of October).

#### 4.1.2. Neap Tide Dynamics

The dynamics in neap tide was influenced by the strong diurnal oscillation of the tidal current (with variations up to 0.5 m/s between two cycles). Its influence was noticeable in the sheared interface. This interface weakened once a day during the inflow phase (first inflow Figure 3c).

During the outflow (16:00 to 23:00 the eleventh), the 50 m thick interface (depicted by isopycnals in Figure 3d) was less turbulent than the surrounding layers, especially the Mediterranean layer where  $\epsilon_E$  reached  $10^{-3} \text{ W}\cdot\text{kg}^{-1}$ . During the inflow, the dissipation varied with the diurnal cycle of the tidal current. In the intensified phase (08:00 to 16:00 the eleventh), the interfacial mixed layer was thicker and deeper with a dissipation rate at  $10^{-5} \text{ W}\cdot\text{kg}^{-1}$  spatially homogeneous with some bursts in the Atlantic layer. In the reduced phase (23:00 the eleventh to 05:00 the twelfth), the interface was thinner and stabilized the flow where low dissipation occurred ( $\approx 10^{-7} \text{ W}\cdot\text{kg}^{-1}$ ). Conversely, the dissipation in the Mediterranean layer kept roughly the same intensity as during the previous outflow.

### 4.1.3. Summary

In summary, the analysis reveals a key feature of turbulence over the main sill: the onset of turbulence is favored by strong westward tidal current. It leads to a double asymmetry between inflow/outflow and neap/spring tide with a slight modulation of the diurnal current on the intensity of the dissipation rate. During tidal outflow, the vertical extent of the highly turbulent region is controlled by the intensity of the stratification at MO3.

The Mediterranean vein is the place of strong turbulence at CS. The variability of the turbulence at depth is directly driven by the strength of the total bottom current composed of the westward Mediterranean outflow superimposed with tidal barotropic current.

### 4.2. Dissipation in the Mediterranean Outflow

The FPO station, performed in neap tide, captured the increase of the Mediterranean outflow along the western flank of CS from tidal inflow to tidal outflow (see Figure 1 for the location). Figure 4 shows the flow evolution from the end of the inflow to the maximal outflow with three CTD casts, p5, p6 and p7. At p5, the Mediterranean outflow was blocked and the current headed east. The echo-sounder revealed no clear interface between upper inflow and lower outflow (Figure 4a); the dissipation rate was  $\epsilon_T \sim 10^{-7} \text{W.kg}^{-1}$  in  $O(10 \text{ m})$  structures (Figure 4b). When the tidal current reversed, the Atlantic inflow was blocked, the Mediterranean outflow accelerated and thickened upwards to a seasonal thermocline at  $\sim 30 \text{ m}$  depth. The echo-sounder identified an acoustic interface (white shade on Figure 4b) collocated with the maximum shear (Figure 4c). At p6, the CTD cast provided a dissipation rate  $10^{-3} \text{W.kg}^{-1}$  in  $O(40 \text{ m})$  tall turbulent patches, in the deepest 300 m of the water column. With the increasing westward tidal current, the Mediterranean outflow grew as illustrated by the rise of the acoustic interface. The maximum shear remained large near 200 m depth. The acoustic back-scatter revealed 100 m amplitude vertical oscillations suggesting Kelvin-Helmholtz (KH) billows. Then (at p7), in the Mediterranean outflow,  $O(70 \text{ m})$  tall structures with turbulent dissipation rates exceeding  $10^{-3} \text{W.kg}^{-1}$  were identified in the deepest 300 m (Figures 4a and 4b). Roustan et al. (2023) interpreted this event as the unsteady detachment of the Mediterranean vein from the slope leading to large overturns.

Figures 4d and 4e describe the water masses with the turbulent diffusivity and the dissipation rate at the three CTD casts, during the tidal cycle. The tidally modified gravity current mixed Mediterranean waters with Atlantic waters when it detached from the slope. Both dissipation rate and diffusivity were weak along the NACW-SAW mixing line ( $\epsilon_{\text{max}} \approx 5.10^{-7} \text{W.kg}^{-1}$ ), compared to those of the mixing line between LIW and NACW (right of the 37.5 isohaline). The NACW had increasing temperature and salinity between p5 and p7 (elbow point in the orange dashed box), corresponding to the highest  $\epsilon_T$ . Thus, the turbulence developed there mixed preferentially the Mediterranean waters with the NACW.

Both the size  $O(70 \text{ m})$  of the turbulent structures, and the dissipation rates  $10^{-3} \text{W.kg}^{-1}$ , observed here, are comparable with those of the 1985/1986 experiments (Armi & Farmer, 1988; Wesson & Gregg, 1994): dissipation rates of  $10^{-2} \text{W.kg}^{-1}$  in structures  $O(75 \text{ m})$  thick during neap tide outflows west of CS. Following Baines (2008), Roustan et al. (2023) hypothesize that the detachment of the Mediterranean waters from the slope explains the overturn at the end of FPO station. As a consequence, the local mixing along the western flank of CS in neap tides affects essentially the Mediterranean waters and the NACW but not SAW.

### 4.3. Hydraulic Jumps and Mixing

The formation of a hydraulic jump during spring tide outflows over CS has already been observed (Armi & Farmer, 1988; Roustan et al., 2023) and modeled (Hilt et al., 2020; Sanchez-Garrido et al., 2011). In spring tide inflows, the existence of a hydraulic jump has been suggested north of CS, by Armi and Farmer (1988); Lafuente et al. (2018). Recently, Roustan et al. (2023) provided evidence for such a jump south and over CS with acoustic images and ADCP measurements. Here, we apply the Thorpe length method to MVP profiles to calculate dissipation rates  $\epsilon_T$ , along sections S2 and S4, in spring tides, respectively during tidal outflow and tidal inflow. Figure 5 (resp. 6) shows (a) an acoustic image from EK60 echo-sounder at 38 kHz, superimposed on the Thorpe length of MVP profiles performed along S2 (resp S4), (b) the vertical shear of the zonal current superimposed on  $\epsilon_T$  and on the normalized profile of centered squared Brunt-Väisälä frequency. The maximum  $N^2$  value is indicated at the top of each profile. The last two panels are T-S diagrams for profiles P1, P4 and P8 (resp. P1 and P7) colored by (c) turbulent diffusivity and (d) turbulent dissipation rates.

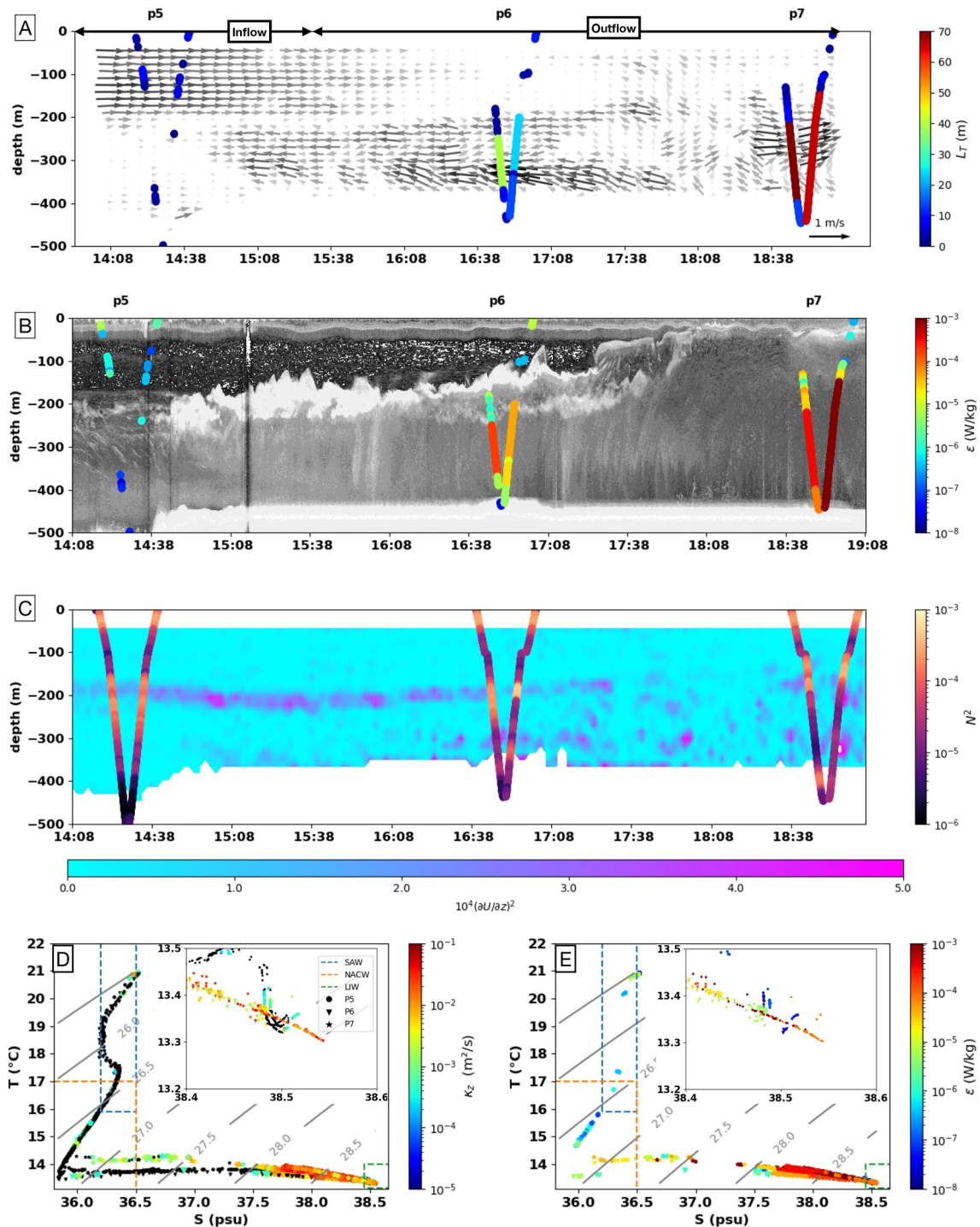


**Figure 4.** (a) Thorpe length  $L_T$  and (b) turbulence dissipation rate  $\epsilon_T$  in turbulent patches along FPO station superimposed over current arrows in the  $u$ - $w$  plane and EK60 acoustic background at 38 kHz (white suggest strong back-scatter) respectively. (c) Vertical shear of the zonal current from OS38 Acoustic Doppler Current Profiler superimposed with squared Brunt-Väisälä frequency  $N^2$  reordered along CTD measurements. (d) Turbulent diffusion rate and (e) turbulent dissipation rates in the T-S diagram, from the CTD measurements. Black dots represent values out of the detected turbulent patches. Insets are zooms on the Mediterranean waters.

Along both sections, dissipation rates were stronger on the lee side of the sill for each phase. The maximal dissipation rate lay in the hydraulic jumps reaching  $10^{-3} \text{ W.kg}^{-1}$  in tidal outflow (P8 Figure 5a) and  $10^{-4} \text{ W.kg}^{-1}$  in tidal inflow (P7 Figure 6a). During tidal outflow, the turbulent patches were  $O(60 \text{ m})$  high versus  $O(10 \text{ m})$  in tidal inflow. Stronger mixing in hydraulic jumps during tidal outflow led to an erosion of NACW along S2 section

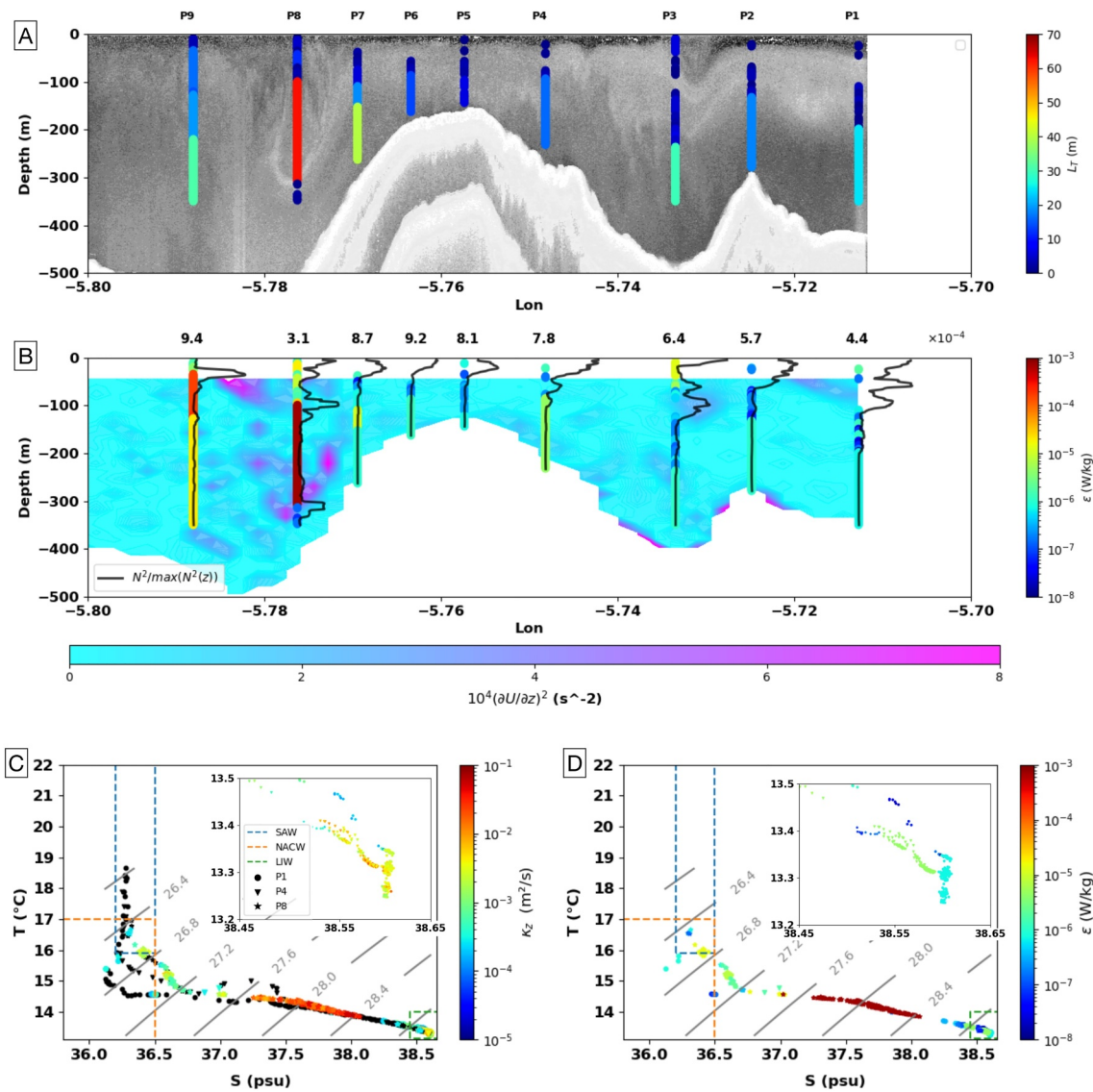


**Figure 5.** (a) Thorpe scale within turbulent patches along S2 section 2 hours before high water (tidal outflow), over EK60 acoustic back-scatter at 38 kHz. (b) Vertical shear of the zonal current squared superimposed with the turbulent dissipation rate  $\epsilon_T$  (colored scatter) and normalized profile of ordered squared Brunt-Väisälä frequency (thin black line). (c) and (d) T-S diagram for profiles 1, 4, and 8 (indicated at the top of panel (A)) colored with turbulent diffusivity and turbulent dissipation rates respectively. Colored rectangular boxes delimit the water masses. Insets are zooms on the Mediterranean waters.

(5c) compared to the inflow (6c). The NACW was a good marker for mixing. Indeed, it formed a thin layer between LIW and SAW that is eroded first by mixing (Macias et al., 2006).

#### 4.3.1. Tidal Outflow Along S2 Section

During the tidal outflow (S2 section Figure 5), the acoustic image depicted a 200 m height overturning structure matching with intense shear and high turbulent dissipation rate  $\sim 10^{-3} \text{W.kg}^{-1}$ . This large overturns trapped Atlantic water inside the Mediterranean waters enhancing the mixing between these water masses (Figures 5c and 5d). This was also evidenced by the two spikes in the stratification profile (black line at P8 in Figure 5a), suggesting advection of Atlantic waters within the Mediterranean vein. In the wake of this overturn (profile P9), two turbulent patches with relatively high dissipation rate ( $\epsilon_T \sim 0.5 - 5 \times 10^{-4} \text{W.kg}^{-1}$ ) suggested that large turbulent structures cascade along the hydraulic jump.

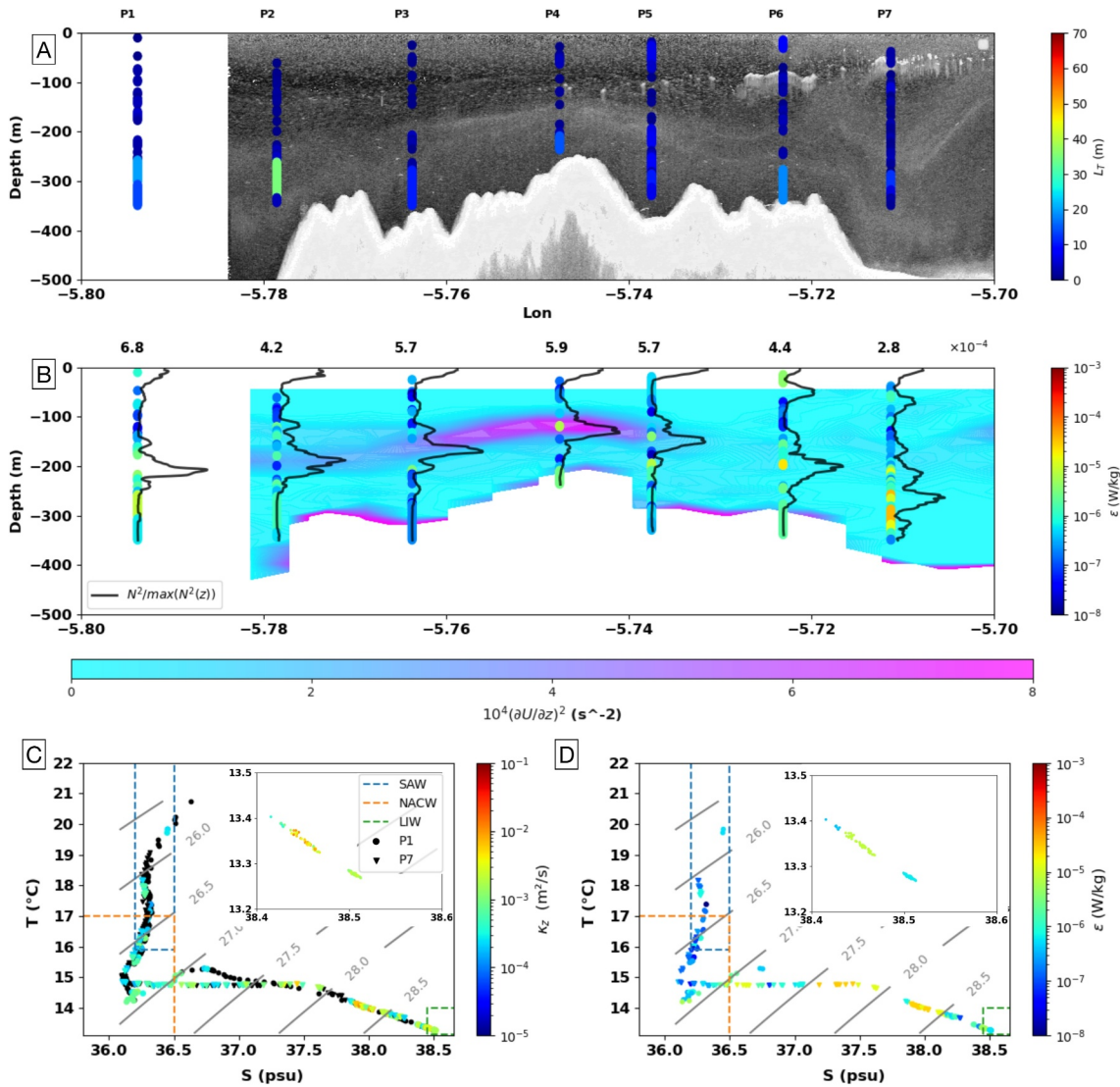


**Figure 6.** (a) Thorpe scale within turbulent patches along S4 section 2 hours before low water (tidal inflow), over EK60 acoustic back-scatter at 38 kHz. (b) Vertical shear of the zonal current superimposed with the turbulent dissipation rate  $\epsilon_T$  (colored scatter) and normalized profile of ordered squared Brunt-Väisälä frequency (thin black line). (c) and (d) T-S diagram for profiles 1 and 7 (indicated at the top of panel (a)) colored with turbulent diffusivity and turbulent dissipation rates respectively. Colored rectangular boxes delimit the water masses. Insets are zooms on the Mediterranean waters.

Between P2 and P3 the acoustic interface showed a disturbance identified as a small hydraulic jump by Roustan et al. (2023). This internal feature was associated with a turbulent dissipation rate of  $5 \times 10^{-6} \text{ W.kg}^{-1}$  below the acoustic interface and  $4 \times 10^{-7} \text{ W.kg}^{-1}$  near the interface (200 m depth). The upper 50 m exhibited intense dissipation rate with  $\epsilon_T$  up to  $2.10^{-5} \text{ W.kg}^{-1}$ . The dissipation rates at P3 were a hundred times smaller than those at P8 in the main hydraulic jump. The core of the hydraulic jump was stable (the acoustic signal at P8 and P3 is another indicator). But at the extremity of the stable core, the enhanced shear and weakened stratification led to bursts of turbulence.

The water masses presented a zonal variability, with a strong erosion of the NACW westward. Indeed, between P1 and P8 the NACW elbow was totally mixed with much saltier waters along 15°C (Figure 5c). This illustrates the ability of unstable hydraulic jumps to connect Mediterranean and Atlantic waters, which can then mix. The mixed water (with  $\sigma$  between 27.5 and 28 kg/m<sup>3</sup>) supported the strongest diffusivity (Figure 5c). Note also that the Mediterranean waters were also strongly impacted by shear instabilities. The low stratification observed there explained the large diffusivity with  $\kappa_z \approx 10^{-2} \text{ m}^2/\text{s}$  despite fairly low turbulent dissipation rates ( $\sim 10^{-6} \text{ W.kg}^{-1}$ ).

### 4.3.2. Tidal Inflow Along S4 Section

During spring tide inflow, the acoustic image depicted an interface oscillating around 200 m depth along the S4 section. This interface was collocated with an intense vertical shear and with stratification maxima (Figures 6a and 6b). On the western part of section S4 (profiles P1 to P5), high vertical shear matched strong stratification leading to Richardson numbers of order one (typically  $Ri = \frac{6 \times 10^{-4}}{6 - 810^{-4}} \approx 1$  between P2 and P5). Therefore, the interface was stable to KH mechanism ( $Ri > 0.25$ ). None or few turbulent patches were detected there. This was consistent with the measurements at MO3 at this stage of the tidal cycle which depicted a relatively quiescent interface (Figure 3c). The sheared interface progressively vanished leeward and maximal turbulence was observed below the hydraulic jump on profile P7 with  $\epsilon_T$  reaching  $5.10^{-5} \text{ W.kg}^{-1}$ .

On profiles P1 and P2, dissipation rate of  $\epsilon_T \sim 10^{-6} - 10^{-5} \text{ W.kg}^{-1}$ , occurred below the main pycnocline (at about 300 m depth). Wesson and Gregg (1994) also reported maximum turbulent dissipation rates on the west flank of CS during tidal inflows. They attributed this enhanced turbulence to the frontal dynamics between the Atlantic waters and the blocked Mediterranean waters. Figure 6b does not evidence a deepening of the pycnocline on the west flank associated to frontal dynamics. Thus the source of this intensified turbulence may have been an increased shear in the Mediterranean outflow or frontal dynamics to the North (near S2 in shallower water). Possibly, high modes of internal tide quickly break leading to enhance turbulence there.

The T-S properties of the water masses remained quite constant along section S4 though smaller temperature at P7 (19°C vs. 21°C elsewhere). High turbulent diffusivity was detected along the NACW-LIW mixing line, but much less along the SAW-NACW mixing line (Figure 6c). This suggests a key role of the advection rather than local mixing in explaining the increase of temperature of the NACW elbow along this section. Previous studies illustrated that part of the Atlantic waters mixed during tidal outflow can be advected eastward during the following tidal inflow (Gonzalez et al., 2023; Lafuente et al., 2013; Macias et al., 2006). Thus, the NACW elbow variability along S4 should have been impacted by both the advection and the tidal outflow mixing of the previous cycle. Finally, the LIW itself was strongly mixed (with  $\kappa_z$  near  $10^{-2} \text{ m}^2/\text{s}$  during this phase) essentially on the western flank of the Sill. The P7 profile might have been too shallow to sample in the LIW on the eastern side of CS. Thus, this observation suggests that eastern hydraulic jump developed during tidal inflow mixed quite well the Atlantic and interfacial mixed waters but not the Mediterranean waters, which underwent intense mixing west of the Sill during their eastward advection.

In summary, hydraulic jumps are places of strongly turbulent flows. The plunge of isopycnals increases the vertical shear of the zonal current and triggers structures up to  $O(60 \text{ m})$  width with  $\epsilon_T$  at  $10^{-3} \text{ W.kg}^{-1}$ . However, the dissipation rates associated to hydraulic jumps present a notable variability regarding the respective position of the stratification and shear. The mixing associated with such processes depends of the size of the turbulent structures and on the local water masses. During tidal outflow, we evidence that Atlantic and Mediterranean waters are directly mixed modifying the NACW properties. Conversely, during tidal inflow, smaller structures mix NACW with interfacial waters. The main outcome is that hydraulic jumps are the only process able to directly mix SAW and NACW with Mediterranean waters while shear-instabilities mix Mediterranean and Atlantic waters only with the interfacial waters (see Section 6 for details).

## 5. Spatio-Temporal Description of the Turbulence in the Vicinity of Camarinal Sill

During PROTEVS GIB20 field campaign various sections were performed over CS (S1, S2, S3, S4 Figure 1) and around it (CS1, CS2, CS3, CS4 Figure 1) at different phases of the fortnightly cycle. In addition, the mooring lines at MO1 and MO3 with high frequency temperature probes give access to the turbulence time evolution during the whole campaign especially in the Mediterranean outflow.

### 5.1. Spatial Description

Figure 7 illustrates the vertically integrated,  $\langle \epsilon_T \rangle$  turbulent dissipation rate, defined as  $\rho_0 \int_{-H}^0 \epsilon_T dz$ , with  $\rho_0 = 1,000 \text{ kg m}^{-3}$ , at different phases of the tidal and fortnightly cycle. It combines all measurements along CTD-MVP profiles in the CS area. Figure 7 reveals the asymmetry between the western and eastern flanks of CS in turbulent dissipation rate. Turbulence was largely intensified on the western slope of the sill during tidal outflows. The influence of the topography is evidenced with intensified turbulent patches (red dots with  $\epsilon_T$  over  $10^2 \text{ W m}^{-2}$ )

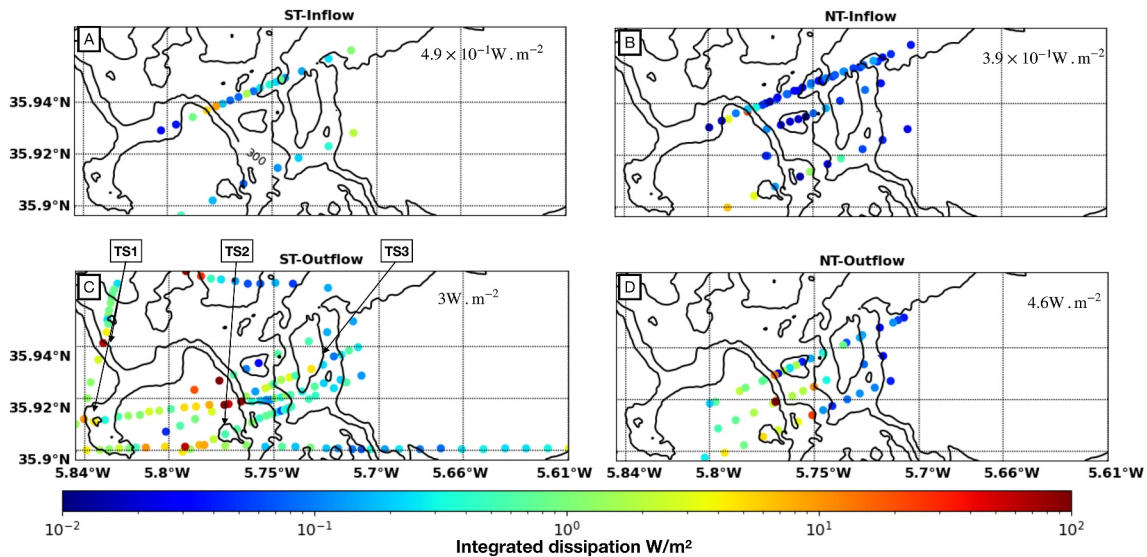


**Figure 7.** Maps of the integrated turbulent dissipation rate  $\langle \epsilon_T \rangle$  along MVP-CTD sections for different situations: (a) spring tides inflows, (b) neap tides inflows, (c) spring tides outflows, (d) neap tides outflows. The spatial averaged value is given in the top right corner of each panel.

located on the lee side of the slopes. The maximum value of  $\langle \epsilon_T \rangle$  is  $1.5 \times 10^2 \text{ W} \cdot \text{m}^{-2}$  during spring tide outflows and  $2.9 \times 10^2 \text{ W} \cdot \text{m}^{-2}$  during neap tide outflows. It never exceeded  $10^1 \text{ W} \cdot \text{m}^{-2}$  during the inflow.

During tidal inflows, integrated dissipation rates were quite similar between spring and neap tides. They slightly increased on the eastern flank of the sill. The spatially averaged  $\langle \epsilon_T \rangle$  varied in  $3.9\text{--}4.9 \times 10^{-2} \text{ W} \cdot \text{m}^{-2}$ . The relatively small  $\langle \epsilon_T \rangle$  during inflow revealed that the vertical extent of the turbulent structures was small at this stage. Indeed, the maximum values were much higher than the medians, with  $\epsilon_{\text{max}} = 1.7 \times 10^{-4} \text{ W} \cdot \text{kg}^{-1}$  during spring tide and  $\epsilon_{\text{max}} = 8.7 \times 10^{-5} \text{ W} \cdot \text{kg}^{-1}$  during neap tide (not shown). Thus, during tidal inflows highly turbulent structures developed but only locally.

During tidal outflows large integrated dissipation rates were found during the whole fortnightly cycle. The strongest values were localized along the slope in neap tide while they extended much westward in spring tide. Another interesting feature observed during spring tide outflow was the strong dissipation rates near small topographic features (identified as TS1, TS2, TS3 on Figure 7c). The matching between these high values and the topographic features suggests topographically driven turbulence like in hydraulic jump structures. The spatially averaged turbulent diffusivity compares well between neap and spring tides.

## 5.2. Temporal Variations of Turbulent Kinetic Energy Dissipation in the Mediterranean Outflow

Turbulent dissipation rates inferred from CTD cast along FPO illustrate intense turbulent events in the Mediterranean outflow on the lee side of the Sill. Now, we address the question of the temporal variations of the turbulence along the slope of the sill. Figure 8 shows the time evolution of the turbulent dissipation rates near the bottom (80 and 15 m above the bottom at (a) MO1 and (b) MO3 respectively) at different phases of the tidal cycle. Intense turbulence occurred at both locations with a strong variability especially during tidal inflow (LW-6 to LW), depending on the tidal strength. The averaged dissipation rate was one order of magnitude higher during tidal outflow (LW to LW+5) compared to tidal inflow. The dissipation rate was one order of magnitude smaller during spring tide inflow than during spring tide outflows. During neap tides  $\epsilon_E$  was less tidally variable (by a factor 2 at most, between tidal inflow/outflow).

During tidal inflows (LW-6 to LW in Figure 8) a significant difference is observed between spring and neap tide dynamics. On average at LW-2 (resp. LW-3), at MO1 (resp. MO3), the turbulent dissipation rate was 10 times smaller than during spring tides. Especially at MO1 this contrast was even larger for the strongest tides; the minimal value was indeed smaller than  $10^{-6} \text{ W} \cdot \text{kg}^{-1}$ . This evidences the ability of strong tidal inflows to stop the Mediterranean outflow drastically reducing the turbulence at depth. On the contrary, with weaker tides, this outflow runs continuously. The 1 hr phase difference between the minima at the two moorings can be explained



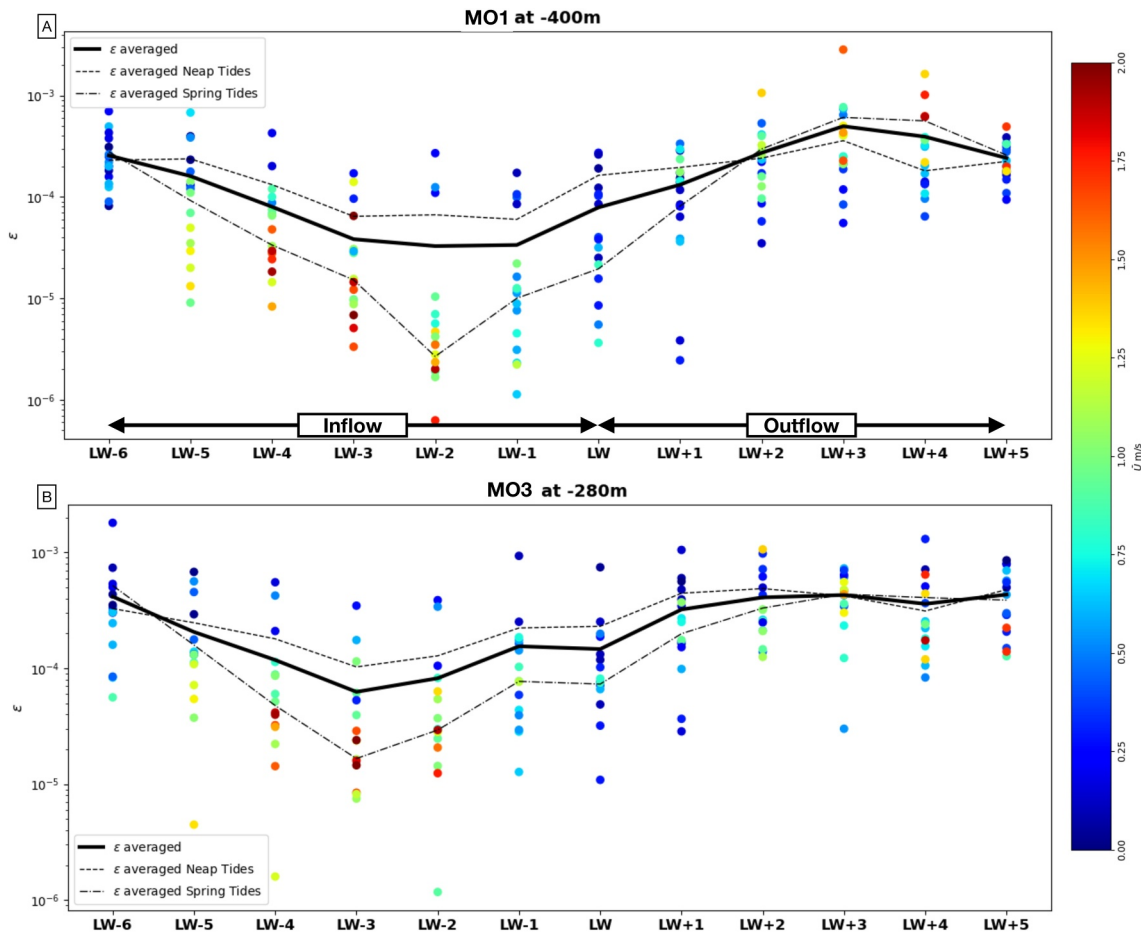


**Figure 8.** Time evolution of the turbulent dissipation rate computed from Ellison number during a tidal cycle, (a) at 400 m depth at MO1, (b) at 280 m depth at MO3. The dotted points correspond to the turbulent dissipation rate computed at each cycle colored by the corresponding barotropic current at MO2 at this phase. The thick black line represents the averaged turbulent dissipation rates over the whole time series. The thin dotted black line is the averaged turbulent dissipation rates during neap tide, the thin dash-dotting black line is the same during spring tide.

by influence of downhill flow at MO1 and not at MO3. As a consequence, the Mediterranean water dynamics at MO3 was dominantly controlled by the tide; while at MO1, the inertia of the dense flow running down-slope was also part of the dynamics. Thus, a stronger tidal current was required to stop the flow at MO1 than at MO3. This shifted the occurrence of minimal turbulence by 1 hour between the two moorings.

During tidal outflows (LW to LW+5 in Figure 8), the turbulent dissipation rate undergoes substantial variations. Still, it is not correlated with the strength of the tide at MO3 whereas it is at MO1. At MO1, the tide intensifies the Mediterranean outflow up to a detachment point. This is suggested by the third CTD sounding during FPO station (see Section 4.2). Over CS, a turbulent bottom boundary layer develops for all tides (Figures 3a–3c); the variability there is attributed to bursts of turbulence.

Time series of the turbulent dissipation rates near the bottom illustrate the high turbulence level developed at CS and on its western slope, with averaged value  $2 \cdot 10^{-4} \text{ W.kg}^{-1}$ . The coupling of the dense gravity current of Mediterranean water with the tidal forcing clearly appears in the level of turbulence. Strong tidal inflows blocking the Mediterranean vein decrease the turbulence near the bottom at both moorings. The possible detachment of the Mediterranean outflow, only observed at MO1, generates turbulent dissipation rates up to  $10^{-3} \text{ W.kg}^{-1}$  in the strongest overturns. Note that both Thorpe and Ellison methods provide the same order of magnitude for the turbulent dissipation rates in the largest turbulent structures.

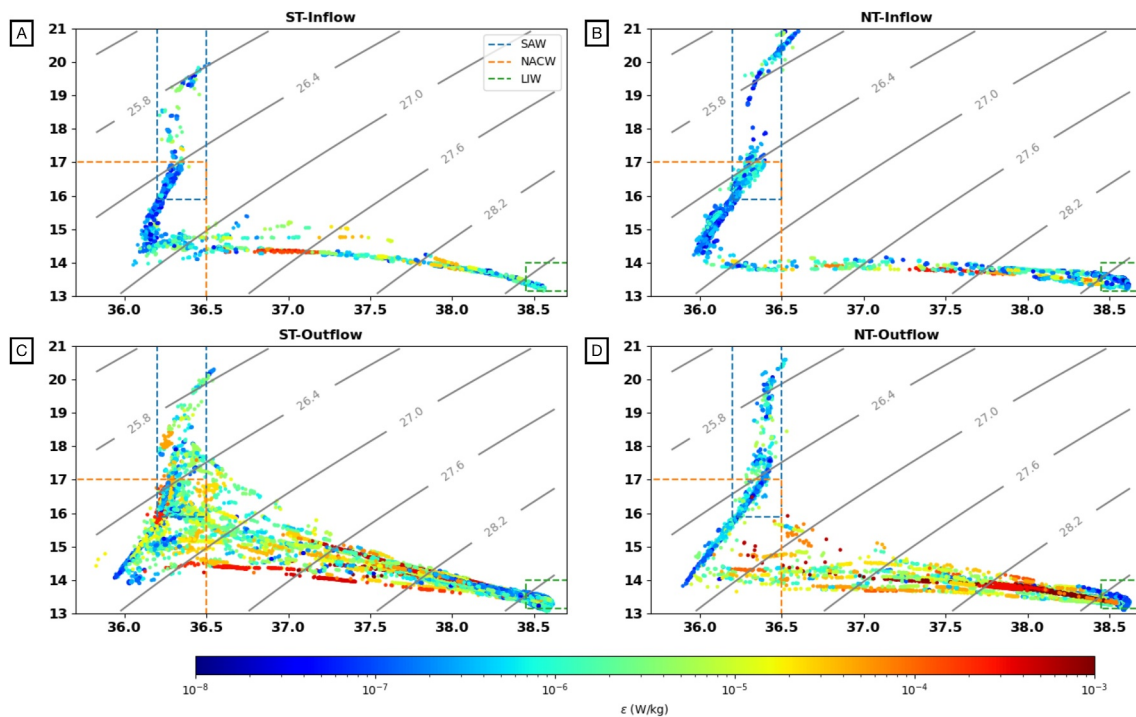


**Figure 9.** TS diagram in the detected turbulent patches with the Thorpe method colored with the associated turbulent dissipation rate for different situations, (a) spring tides inflows, (b) neap tides inflows, (c) spring tides outflows, (d) neap tides outflows.

### 5.3. Summary

The integrated turbulent dissipation rates exhibit a spatial asymmetry near CS, the western flank being much more turbulent. On top of this asymmetry, the flow is 10 times more turbulent during tidal outflow than in tidal inflow. This is due to the baroclinic large-scale circulation with the deepest layer (the Mediterranean vein) flowing westward. The integrated dissipation is slightly modulated by the fortnightly cycle.

At depth, we evidence the complex interaction between the Mediterranean overflow and the tidal current which strongly modulates the turbulent dissipation rate. Increasing eastward tidal currents dramatically reduce the kinetic dissipation as they block the Mediterranean overflow. Conversely, increasing westward tidal currents increase  $\epsilon$ . Therefore, spring tide outflows are characterized by a larger tidal variability of  $\epsilon$  compared with neap tide outflows.

## 6. Impact of Turbulence on Water Mass Properties Above Camarinal Sill

The PROTEVS GIB20 data set exhibits intense turbulent dissipation rates over CS, where Atlantic and Mediterranean waters encounter. In the following we study the influence of such rapidly varying turbulence on the water mass properties.

Figure 9 presents T-S diagrams colored with the turbulent dissipation rates calculated along MVP-CTD sections for (A/B) spring/neap tide inflows, (C/D) spring/neap tide outflows. Both the fortnightly and tidal cycles strongly impact the water masses over the sill. The main result is the difference in the T-S spreading between tidal inflow and tidal outflow. During tidal inflow, T-S diagrams fit quite well with NACW-SAW and SAW-LIW mixing lines (Figures 9a and 9b) while during tidal outflow T-S points are more spread out, suggesting a three-way mixing (Figures 9c and 9d). Note that three-way mixing affects T-S properties between NACW, SAW and LIW, such that it lies in the triangle between LIW-NACW, NACW-SAW and SAW-LIW mixing lines in a T-S diagram.

During tidal inflows, small turbulent patches with typical dissipation rate of  $5 \cdot 10^{-7} \text{ W} \cdot \text{kg}^{-1}$  were detected along the NACW-SAW mixing line (Figures 9a and 9b). Stronger  $\epsilon$  were observed along the mixing line between the NACW and the LIW arguing for local mixing at the interface due to small shear overturns. Small dissipation rates

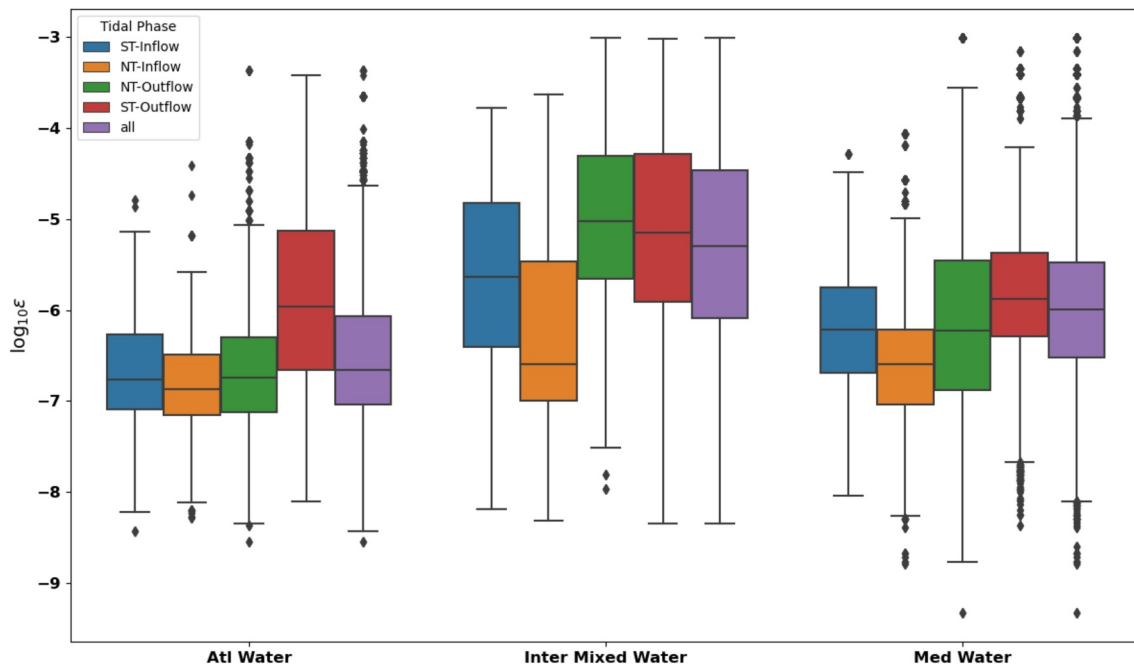


**Figure 10.** Statistics of the turbulent dissipation rate at different stages of the fortnightly and diurnal tidal cycles for the three typical water masses in the SoG: The Atlantic Water, the Mediterranean Water and the intermediate waters. The water masses are defined by the salinity (see text). The boxes represent 75% of the values between the first quartile  $Q_1$  and the third quartile  $Q_3$ . The outliers are values outside of the frame  $[Q_1 - 1.5(Q_3 - Q_1), Q_3 + 1.5(Q_3 - Q_1)]$ .

were detected in the warmer waters, which were under the influence of atmospheric forcing. These turbulent patches were likely wind induced turbulence, but this is out of the scope of this study.

During tidal outflows, turbulence spread out T-S properties of water masses between the NACW, the SAW and the LIW, in particular during spring tide outflows (Figure 9c). High  $\epsilon$  values ( $3 \times 10^{-4} \text{ W.kg}^{-1}$ ) were found at the edges of the triangle. During neap tide, the strongest  $\epsilon$  values were observed along the NACW-LIW mixing line. The T-S diagram was less spread out, which confirmed that SAW and LIW were hardly mixed in neap tide despite integrated turbulent dissipation rates comparable with those observed in spring tides.

To summarize these observations, we provide the statistics of the dissipation rates in three water masses, the Atlantic waters, the interfacial mixed waters and the Mediterranean waters. The isohaline 36.5 psu is a limit between Atlantic and interfacial mixed waters and 38 psu between interfacial and Mediterranean waters. Figure 10 shows the turbulent dissipation rates (along CTD-MVP sections) during the tidal/fortnightly cycle.

First, note that Atlantic waters were less impacted by turbulent processes with an average  $\epsilon$  of  $2 \times 10^{-7} \text{ W.kg}^{-1}$ . During spring tide outflow, the Atlantic waters were more mixed than during the other phases; the median dissipation rate was one order of magnitude higher. Interfacial mixed waters underwent high dissipation in all situations; the global dissipation rate was  $7 \times 10^{-6} \text{ W.kg}^{-1}$ . The highest dissipation rates in this water mass were observed during tidal outflows ( $\epsilon$  about  $10^{-5} \text{ W.kg}^{-1}$ ) without significant differences between spring and neap tides. Finally, the Mediterranean waters had intermediate dissipation rates between these two extremes,  $\epsilon \sim 10^{-6} \text{ W.kg}^{-1}$ .

In the Mediterranean waters, the variability was less pronounced, even if the dissipation rate appeared enhanced during tidal outflows. During tidal inflows, the dissipation rate was significantly smaller in neap tide than in spring tide, opposite to what happened at depth (Figure 8). However, this statistical view does not account for the spatial position as it aggregates data from all around CS. Indeed, when selecting only casts west of  $-5^\circ 75' \text{ W}$ , we recover stronger turbulent dissipation rates in the Mediterranean waters during neap tide inflows. This evidences the dual role of tide and gravity in the dynamics of the Mediterranean outflow west of CS. This result supports the previous finding of Wesson and Gregg (1994) with similar turbulent levels between neap and spring tide outflows except for the Atlantic water. Thus, different processes trigger these high turbulent dissipation rates. During

spring tides, hydraulic jumps develop along the interface while during neap tides the largest vortices are located below the interface in the Mediterranean layer, the former being thus more efficient in mixing the Atlantic waters.

## 7. Discussion and Conclusions

### 7.1. Limits and Uncertainties

The main limitations of our computations result from the sampling rate of the sensors and the intrinsic assumptions of each method. For the Thorpe length method, the range of vertical overturn is limited by the minimum  $\Delta\rho$  imposed to avoid false overturns. At fixed  $N^2$ , it gives  $\Delta z = \frac{g}{\rho_0} \frac{\Delta\rho}{N^2}$ , leading to a minimum value for  $\epsilon_T \geq 0.64 \frac{g}{\rho_0} \Delta\rho N \sim 10^{-10} \text{Wkg}^{-1}$ . The method holds when stratification limits the size of the turbulent structure, which is expected everywhere except in homogeneous BBL. Wesson and Gregg (1994) showed that  $0.25L_T \leq L_O \leq 4L_T$  from direct micro-structure measurements. Therefore,  $\epsilon_T$  is accurate to an order of magnitude. The Ellison scale requires some choice of cutting frequency and average time scale that have been shown to have little impact on the result (See appendix A for complete discussion). Despite these limitations, the two methods allow us to infer reliable  $\epsilon$  in different regimes.

### 7.2. Camarinal Sill, Just One of Many?

These observations confirm that the SoG, especially CS, is a very turbulent area. With the Thorpe length method, we calculated turbulent dissipation rates of about  $10^{-3} \text{W.kg}^{-1}$  in overturns  $O(70 \text{ m})$  tall. This is in good agreement with the findings of Wesson and Gregg (1994) who, in their pioneering study, reported maximal  $\epsilon$  of  $10^{-2} \text{W.kg}^{-1}$  in  $O(75 \text{ m})$  overturns. High turbulence levels were due to different dynamical processes which develop at different locations of CS during the tidal/fortnightly cycle: bottom boundary layer over the sill, shear instability at the interface between Atlantic and Mediterranean Waters, hydraulic jumps, overturns in the Mediterranean outflow on the western flank of CS.

The turbulent dissipation rate over CS strongly varies with tide. In this sense, the Mediterranean overflow behaves quite differently from abyssal density-driven overflows like in the Samoan passage where turbulence is persistent (Cusack et al., 2019). However, when the flow is controlled over CS the turbulent dynamics fits relatively well with the three regimes previously described by the authors. Windward the sill the flow is relatively quiescent ( $\epsilon \sim 5 \cdot 10^{-7} \text{W.kg}^{-1}$ ), in the supercritical flow over CS the turbulence developed over the interface and in the Mediterranean overflow ( $\epsilon \sim 10^{-4} \text{W.kg}^{-1}$ ) and leeward intense turbulence develops in an unstable hydraulic jump ( $\epsilon \sim 10^{-3} \text{W.kg}^{-1}$ ). In any case, the dissipation rates observed in the SoG are three orders of magnitude larger than in the Samoan passage. Similarly with the Samoan passage, CS is characterized by multiple topographic accidents with different levels of turbulence (Carter et al., 2019). Conversely to the Samoan passage, the flow over each topographic feature at CS is locally supercritical at the maximum tidal outflow and hydraulic jumps are observed leeward (Roustan et al., 2023). This evidences a large variation of turbulence in hydraulic jumps, defined as the transition from supercritical to subcritical flow. Pratt and Whitehead (2008) recalled that the flow becomes unstable when it is supercritical and the bulk Richardson number  $R_b = \frac{g'H}{|u_1 - u_2|}$  - with  $g' = g\Delta\rho/\bar{\rho}$  the reduced gravity,  $H$  the water depth,  $u_1$ ,  $u_2$  the current in the upper/lower layer - lies below unity. A rough estimate of  $R_b$  at profile P3 and P8 of section S2 gives approximately 1.45 and 0.87 respectively, suggesting stable/unstable flows at P3/P8, which are effectively observed. We used  $u_1 = 0 \text{ m/s}$  at each profile and  $u_2 = 1 \text{ m/s}$  respectively  $u_2 = 2 \text{ m/s}$  for the computation.

The bottom layer over CS is very turbulent ( $\epsilon > 10^{-3} \text{W.kg}^{-1}$  at MO3) and varies with the intensity of the westward current, sum of tidal current and Mediterranean overflow. The latter acts like a tidally modified gravity current (Roustan et al., 2023). The turbulence in the BBL behaves as in other tidal channels with variations of several orders of magnitude during one tidal cycle (McMillan et al., 2016); but the absolute values are quite large compared with the Grand Passage (Canada) where a similar tidal current of  $2 \text{ m/s}$  develops (McMillan et al., 2016). This highlights the role of the baroclinic flow (and possibly strong macro-topographic rugosity) in the onset of turbulence at depth. However, our deepest measurement were located at  $280 \text{ m}$  depth at MO3,  $15 \text{ m}$  above the bottom. Roustan et al. (2023) reported a  $30 \text{ m}$  thick bottom layer at MO2 which is located in shallower are were tidal current is certainly stronger. Therefore, we can not guarantee that we measured the turbulence level in the core of the BBL. Other measurements in the BBL are needed to draw definitive conclusion on the turbulence level develop in the BBL over CS.

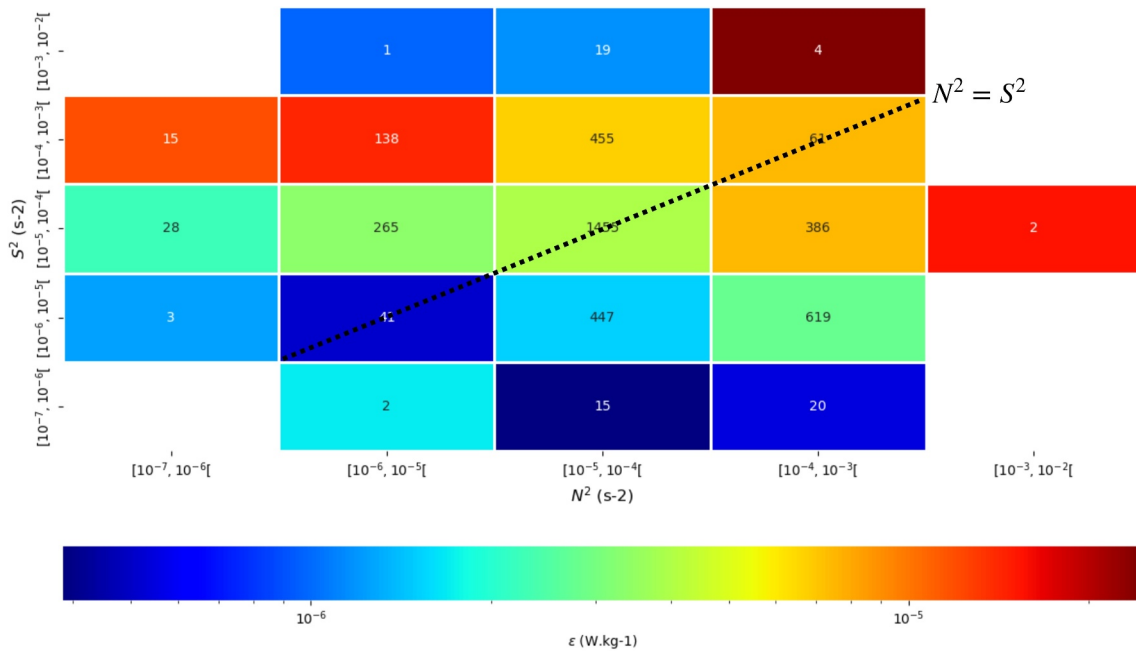


**Figure 11.** Averaged  $\epsilon$  values in turbulent patches averaged by bins of  $N^2$ ,  $S^2$ . In each cell we give the number of detected patches at this location in the map. For each turbulent patch detected with the Thorpe length method in CTD-MVP measurements we computed the averaged squared vertical shear  $S^2 = (\partial U/\partial z)^2 + (\partial V/\partial z)^2$  and the averaged squared ordered Brunt-Väisälä frequency  $N^2 = -\frac{g}{\rho_0} \partial_z \rho_{ordered}$ .

Far from the bottom, the onset of turbulence depends on the criticality of the flow. In spring tide outflows, intense turbulence develops in the whole water column under supercritical conditions while it remains localized below the pycnocline in neap tide subcritical conditions. During tidal inflow, the flow is more quiescent and the turbulence varies with diurnal oscillations of the tidal current. In Knight Inlet (Canada), Klymak and Gregg (2004) evidenced a similar turbulent dynamics with a relative symmetry between ebb and flood. Conversely, in the Oslofjord (Norway), Staalstrom et al. (2015) evidenced inhibition of the hydraulic control during some flood due to variations of the mean baroclinic exchange. Similarly, the turbulent dynamics in the SoG is both controlled by the long-term baroclinic exchange and the intense tidal current.

From a 1 km resolution model, Gonzalez et al. (2023) investigated the drivers of the variability near CS. The authors reported that near the bottom the shear was the dominant process, while near the interface between Mediterranean and Atlantic waters, the variability of the stratification modulated the onset of shear instability and thus the turbulent mixing. These conclusions fit well with our results at MO2/MO3. Near the bottom, the turbulence is intensified by strong westward tidal current increasing the shear. The onset of turbulence in the interfacial layer strongly depends on the local stratification which may or may not be able to stabilize the flow.

To investigate the driver of the turbulence, we plot the averaged  $\epsilon_T$  in turbulent patches by bins of  $S^2$ ,  $N^2$ , where  $S^2 = (\partial_z u)^2 + (\partial_z v)^2$  the squared of the vertical shear of the horizontal currents and  $N^2 = -\frac{g}{\rho_0} \partial_z \rho_{ordered}$  the buoyancy frequency squared of reordered density profiles (Figure 11). It clearly shows that the highest dissipation rates fell where  $S^2 > 10 \times N^2$  suggesting that shear instabilities is the main driver of turbulence. An exception to this rule was one cell with 386 turbulent patches and high  $\epsilon$ . In this specific case, shear instability should not have occurred, at least locally. Two hypotheses might account for this observation. First, high-mode breaking internal waves might result in such turbulent patches as observed in West Espartel Sill (Nash et al., 2012). Second, the turbulent patches might have been generated in unstable environment and advected westward in a stable flow where there have been measured.

### 7.3. Influence of the Turbulence Dynamics Over the Regional Circulation

In their pioneering study, Wesson and Gregg (1994) found averaged dissipation rates on the same order of magnitude between neap and spring tide, typically  $\sim 10^{-5}$  W.kg $^{-1}$ . Our analysis mostly draws similar

conclusions. Slight differences are noted. The vertically integrated dissipation rate underwent tidal modulation, being increased ten-fold in outflow (Figure 7). The spatially averaged integrated dissipation rate showed quite similar values along the fortnightly cycle, even if the location of turbulence hotspots varied. Considering the effect on water masses, the dissipation rate was statistically similar for neap and spring tides in the Mediterranean waters ( $\sim 10^{-6}$  W.kg $^{-1}$ ) and in the interfacial waters ( $\sim 10^{-5}$  W.kg $^{-1}$ ). It was significantly enhanced during spring tide outflows in the Atlantic waters in agreement with the findings of Wesson and Gregg (1994). This latter finding can be due to the variety of dynamical processes triggering turbulence at CS. The structures generated in spring tide outflows, hydraulic jumps typically, directly affect the Atlantic waters and thus favor mixing. This was shown by the T-S spreading (with NACW erosion) in spring tide outflows compared with neap tide (Figures 2c and 2d).

The mixing dynamics over CS drives the hydrographical properties of both the incoming Atlantic jet and the outgoing Mediterranean outflows. An active debate is the ability to detect the original properties of the Mediterranean waters on the western side of the Sill (Millot, 2014, 2017; Naranjo et al., 2014, 2015). We previously reported how the T-S diagram is impacted by the strength and the phase of the tidal cycle with turbulence acting differently on the water masses in the area. Tidal variability should strongly influence the Mediterranean outflow properties detected westward and thus our ability to differentiate water masses in the Mediterranean vein. In addition, we highlighted a spatial variability of the mixing at CS; therefore, the properties of the outgoing water masses should depend on their path when flowing over CS.

At West Espartel Sill, 70 km westward of CS, Nash et al. (2012) evidenced time-varying turbulent dissipation rate in the Mediterranean overflow ( $\epsilon \sim 10^{-5}$  W.kg $^{-1}$ ). At this location high  $\epsilon$  were observed throughout the tidal cycle but their vertical extent follows the tidal variations of the Mediterranean outflow thickness. The authors argued that the Mediterranean outflow behaves like quiescent overflows with localized mixing at specific location with rough topography. Considering the turbulent levels at CS ( $\epsilon \sim 10^{-3}$  W.kg $^{-1}$  up to  $\epsilon \sim 10^{-2}$  W.kg $^{-1}$  following Wesson and Gregg (1994)), the hydrographical properties of the Mediterranean overflow are probably the most conditioned there (Millot, 2014, 2017; Naranjo et al., 2014, 2015). In agreement with Nash et al. (2012) findings, we show that the water masses properties strongly depend on the dynamics of the flow; especially the presence of a large hydraulic jump directly mixing Atlantic waters with Mediterranean waters. Such a process is mainly driven by the balance between stratification and current velocity. In the near future, stratification conditions as well as background flow (García-Lafuente et al., 2021) might change under changing climate, with possible implications on the properties of the Mediterranean outflow and therefore on the Atlantic Meridional Overturning Circulation (Artale et al., 2002; Papadakis et al., 2003).

The exchange flow in straits, fjords and estuaries have long been described through the hydraulic theory, first by Stommel and Farmer (1952); Stommel and Farmer (1953). Later, Armi and Farmer (1985); Armi and Farmer (1986) described the exchange flow in the SoG from this theory. They hypothesized that maximal exchange which requires hydraulic control at Tarifa narrows and CS. Armi and Farmer (1988) confirmed hydraulic control at Tarifa narrows, but they were not able to draw any definitive conclusions at CS. Based on the PROTEVS GIB20 field experiment, Roustan et al. (2023) showed that CS is locally subcritical at some stage of the fortnightly cycle but the experiment was not design to address this question as the sections were focused near CS. In this study we evidence a slight fortnightly modulation of the turbulent mixing especially for the Atlantic waters. The stratification in the SoG certainly varies at this time-scale with possible impact on the exchange flow. Previous studies evidenced that weaker exchange flow during spring tide attributed to enhanced tidal mixing during spring tides (Candela et al., 1989; Roustan et al., 2023; Vargas et al., 2006).

#### 7.4. The SoG, a Challenge for Modeling ?

Our results highlight the four dimensional variability of turbulence in the CS region. This study confirms that the tide drives the variations of the turbulent dissipation rate at first order (Naranjo et al., 2014; Sannino et al., 2015). Therefore, it is a real challenge for climate models, without tide, to adequately parameterize the mixing variability in the SoG. At the regional scale, models of typically  $\sim 1$  km resolution (Gonzalez et al., 2023; Sanchez-Roman et al., 2018; Sannino et al., 2007) can include the tide. Such models should correctly reproduce the mixing in the BBL with a suitable closure scheme. But parameterizing the variability of dissipation in hydraulic jumps (with 1 km horizontal extent) is more challenging. Recent efforts have been successful in reproducing the largest turbulent structures in non-hydrostatic numerical models (Hilt, 2022; Hilt et al., 2020; Sanchez-Garrido

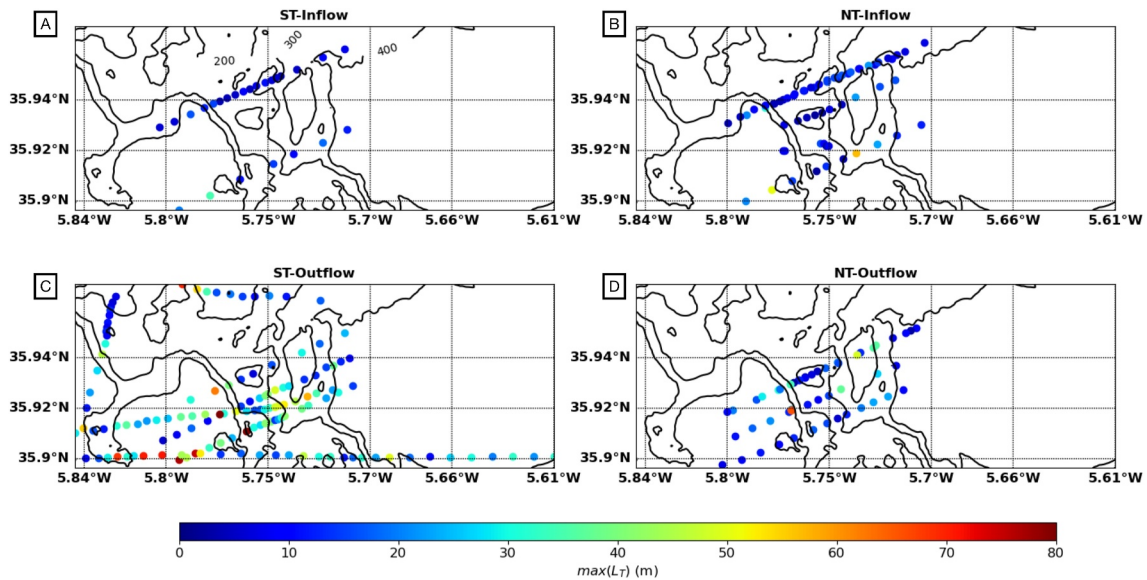


**Figure 12.** Maps of the maximum Thorpe length along vertical profiles of the MVP-CTD sections for the different tidal phases.

et al., 2011). Diapycnal mixing has to be parameterized for the smallest structures. Figure 12 shows the maximum Thorpe length-scale in the turbulent patches along our CTD-MVP profiles. Most turbulent structures are smaller than 10 m, except in spring tide outflows where the structures reach a few tens of meters. With the vertical resolution of the highest-resolution models run until now (7.5 m in the shallowest 300 m (Sanchez-Garrido et al., 2011) or 6 m over CS (Hilt, 2022; Hilt et al., 2020)), the largest turbulent structures can be reproduced during part of the tidal cycle at least in the water column. As far as we know, previously run models are based on RANS turbulence scheme closure. Our findings suggest to move to hybrid, scale-adaptive RANS-LES approaches driven by the characteristics of the turbulent structures (Bechmann et al., 2007; Perot & Gadebusch, 2009).

### Appendix A: Sensitivity Tests for Ellison Length Method

The Ellison length method is sensitive to different parameters: the cutoff frequency used to generate the high frequency temperature fluctuations and the length of the size window over which they are averaged. Our results show that the inferred  $\epsilon$  is quite sensitive to the first parameter when its values overpass the Brunt-Väisälä frequency ( $N \sim 10^{-2}$  Hz); then, internal wave fluctuations might alter the results (Figure A1a). The length of the time window is less sensitive; the amplitude and phasing of the inferred  $\epsilon_E$  slightly varies when the window grows from 2 min to 30 min. However, increasing the size of the window should filter the burst of turbulence and slightly biased the variations (Figure A1b).

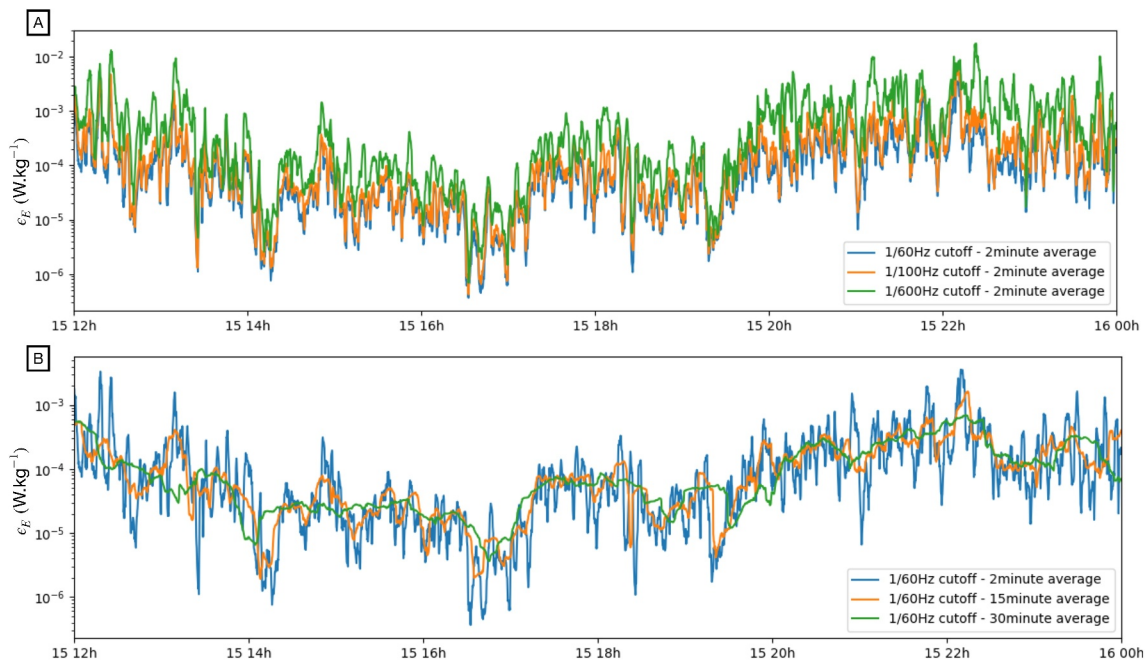


**Figure A1.** (a)  $\epsilon_E$  computed with different cutoff frequencies for the temperature high pass filter. (b)  $\epsilon_E$  computed with different lengths of sliding window for the high frequency temperature average.

## Data Availability Statement

The PROTEVS GIB 20 data used in this paper are available via this link <https://www.seanoe.org/data/00819/93129/> (Bordois & Dumas, 2023).

## Acknowledgments

We gratefully acknowledge the Direction Générale de l'Armement which funded the program Protevs II into which the GIB20 experiment at sea was scheduled, the French Naval Hydrographic and Oceanographic Service (SHOM), the "Flotte Oceanographique Française," FOF and the crew of the R/V "L'Atalante" (IFREMER) for their contribution to the GIB20 experiment preparation and implementation at sea. The SHOM teams in charge of the data collection and their quality control are thanked for their contributions.

## References

- Armi, L., & Farmer, D. (1985). The internal hydraulics of the Strait of Gibraltar and associated sills and narrows. *Oceanologica Acta*, 8(1), 37–46.
- Armi, L., & Farmer, D. (1986). Maximum two-layer exchanged over a sill and through the combination of a sill and contraction with barotropic flow. *Progress in Oceanography*, 21, 1–105.
- Armi, L., & Farmer, D. (1988). The flow of Atlantic Water through the Strait of Gibraltar. The flow of Mediterranean Water through the Strait of Gibraltar. *Progress in Oceanography*, 21, 1–105.
- Artale, V., Calmanti, S., & Sutera, A. (2002). Thermohaline circulation sensitivity to intermediate-level anomalies. *Tellus A: Dynamic Meteorology and Oceanography*, 54(2), 159–174. <https://doi.org/10.3402/tellusa.v54i2.12130>
- Baines, P. G. (2008). Mixing in downslope flows in the ocean – Plumes versus gravity currents. *Atmosphere-Ocean*, 46(4), 405–419. <https://doi.org/10.3137/ao925.2008>
- Bechmann, A., Sørensen, N., Johansen, J., Vinther, S., Nielsen, B., & Botha, P. (2007). Hybrid rans/les method for high Reynolds numbers, applied to atmospheric flow over complex terrain. *Journal of Physics: Conference Series*, 75, 012054. <https://doi.org/10.1088/1742-6596/75/1/012054>
- Bordois, L., & Dumas, F. (2023). Protevs gib20 – Camarinal sill [dataset]. <https://doi.org/10.17882/93129>
- Bouffard, D., & Boegman, L. (2013). A diapycnal diffusivity model for stratified environmental flows. *Dynamics of Atmospheres and Oceans*, 61, 14–34. <https://doi.org/10.1016/j.dynatmoce.2013.02.002>
- Bouruet-Aubertot, P., Cuyper, Y., Ferron, B., Dausse, D., Menage, O., Atmadipoera, A., & Jaya, I. (2018). Contrasted turbulence intensities in the Indonesian Throughflow: A challenge for parameterizing energy dissipation rate. *Ocean Dynamics*, 68(7), 779–800. <https://doi.org/10.1007/s10236-018-1159-3>
- Bryden, H. L., Candela, J., & Kinder, T. H. (1994). Exchange through the Strait of Gibraltar. *Progress in Oceanography*, 33(3), 201–248. [https://doi.org/10.1016/0079-6611\(94\)90028-0](https://doi.org/10.1016/0079-6611(94)90028-0)
- Candela, J., Winant, C. D., & Bryden, H. L. (1989). Meteorologically forced subinertial flows through the Strait of Gibraltar. *Journal of Geophysical Research*, 94(C9), 12667–12679. <https://doi.org/10.1029/jc094ic09p12667>
- Candela, J., Winant, C. D., & Ruiz, A. (1990). Tides in the Strait of Gibraltar. *Journal of Geophysical Research*, 95(C5), 7313–7335. <https://doi.org/10.1029/jc095ic05p07313>
- Carter, G. S., Voet, G., Alford, M. H., Girton, J. B., Mickett, J. B., Klymak, J. M., et al. (2019). A spatial geography of abyssal turbulent mixing in the Samoan passage. *Oceanography*, 32(4), 194–203. <https://doi.org/10.5670/oceanog.2019.425>
- Cimatoribus, A., Haren, H. V., & Gostiaux, L. (2014). Comparison of Ellison and Thorpe scales from Eulerian ocean temperature observations. *Journal of Geophysical Research: Ocean*, 119(10), 7047–7065. <https://doi.org/10.1002/2014jc010132>
- Cusack, J. M., Voet, G., Alford, M. H., Girton, J. B., Carter, G. S., Pratt, L. J., et al. (2019). Persistent turbulence in the Samoan passage. *Journal of Physical Oceanography*, 49(12), 3179–3197. <https://doi.org/10.1175/JPO-D-19-0116.1>



- Dillon, T. M. (1982). Vertical overturns: A comparison of Thorpe and Ozmidov length scales. *Journal of Geophysical Research*, 87(C12), 9601–9613. <https://doi.org/10.1029/jc087ic12p09601>
- Ferron, B., Bouruet Aubertot, P., Cuypers, Y., Schroeder, K., & Borghini, M. (2017). How important are diapycnal mixing and geothermal heating for the deep circulation of the Western Mediterranean? *Geophysical Research Letters*, 44(15), 7845–7854. <https://doi.org/10.1002/2017GL074169>
- Ferron, B., Mercier, H., Speer, K., Gargett, A., & Polzin, K. (1998). Mixing in the Romanche fracture zone. *Journal of Physical Oceanography*, 28(10), 1929–1945. [https://doi.org/10.1175/1520-0485\(1998\)028<1929:mitrfz>2.0.co;2](https://doi.org/10.1175/1520-0485(1998)028<1929:mitrfz>2.0.co;2)
- García-Lafuente, J., Sammartino, S., Huertas, I. E., Flecha, S., Sánchez-Leal, R. F., Naranjo, C., et al. (2021). Hotter and weaker Mediterranean outflow as a response to basin-wide alterations. *Frontiers in Marine Science*, 8. <https://doi.org/10.3389/fmars.2021.613444>
- Gargett, A., & Garner, T. (2008). Determining Thorpe scales from ship-lowered CTD density profiles. *Journal of Atmospheric and Oceanic Technology*, 25(9), 1657–1670. <https://doi.org/10.1175/2008jtecho541.1>
- Gonzalez, N., Waldman, R., Sannino, G., Giordani, H., & Somot, S. (2023). Understanding tidal mixing at the Strait of Gibraltar: A high-resolution model approach. *Progress in Oceanography*, 212, 102980. <https://doi.org/10.1016/j.pocean.2023.102980>
- Hilt, M. (2022). Exploration des fines échelles océaniques dans le détroit de Gibraltar: Simulation numérique, observation et mélange induit.
- Hilt, M., Auclair, F., Benshila, R., Bordoïs, L., Capet, X., Debreu, L., et al. (2020). Numerical modelling of hydraulic control, solitary waves and primary instabilities in the Strait of Gibraltar. *Ocean Modelling*, 151, 101642. <https://doi.org/10.1016/j.ocemod.2020.101642>
- Jordà, G., Von Schuckmann, K., Josey, S., Caniaux, G., García-Lafuente, J., Sammartino, S., et al. (2017). The Mediterranean Sea heat and mass budgets: Estimates, uncertainties and perspectives. *Progress in Oceanography*, 156, 174–208. <https://doi.org/10.1016/j.pocean.2017.07.001>
- Kinder, T. H., & Bryden, H. L. (1987). The 1985–1986 Gibraltar experiment: Data collection and preliminary results. *EOS*, 68(40), 786–794. <https://doi.org/10.1029/eo068i040p00786>
- Klymak, J. M., & Gregg, M. C. (2004). Tidally generated turbulence over the knight inlet sill. *Journal of Physical Oceanography*, 34(5), 1135–1151. [https://doi.org/10.1175/1520-0485\(2004\)034<1135:TGTOTK>2.0.CO;2](https://doi.org/10.1175/1520-0485(2004)034<1135:TGTOTK>2.0.CO;2)
- Lacombe, H., & Richez, C. (1982). The regime of the Strait of Gibraltar. In *Hydrodynamics of semi-enclosed seas* (Vol. 34, pp. 13–73). [https://doi.org/10.1016/S0422-9894\(08\)71237-6](https://doi.org/10.1016/S0422-9894(08)71237-6)
- Lafuente, J. G., Almazán, J., Castillejo, F., Khribeche, A., & Hakimi, A. (1990). *International Hydrographic Review*, LXVII(1).
- Lafuente, J. G., Fanjul, E. A., Vargas, J., & Ratsimandresy, A. (2002). Subinertial variability in the flow through the Strait of Gibraltar. *Journal of Geophysical Research*, 107(C10), 3168. <https://doi.org/10.1029/2001jc001104>
- Lafuente, J. G., Pozas, E. B., Sánchez-Garrido, J. C., Sannino, G., & Sammartino, S. (2013). The Mediterranean Outflow in the Strait of Gibraltar and its connection with upstream conditions in the Alborán Sea. *Journal of Marine Systems*, 117–118, 31–42. <https://doi.org/10.1016/j.jmarsys.2013.02.014>
- Lafuente, J. G., Sammartino, S., Sánchez-Garrido, J. C., & Naranjo, C. (2018). Asymmetric baroclinic response to tidal forcing along the main sill of the Strait of Gibraltar inferred from mooring observations. In *The Ocean in motion* (pp. 193–210). Springer.
- Lafuente, J. G., Sánchez-Román, A., Naranjo, C., & Sánchez-Garrido, J. C. (2011). The very first transformation of the Mediterranean outflow in the Strait of Gibraltar. *Journal of Marine Systems*, 116(C7). <https://doi.org/10.1029/2011jc006967>
- Lafuente, J. G., Vargas, J. M., Plaza, F., Sarhan, T., Candela, J., & Bascheck, B. (2000). Tide at the eastern section of the Strait of Gibraltar. *Journal of Geophysical Research*, 105(C6), 14197–14213. <https://doi.org/10.1029/2000JC900007>
- Macías, D., García, C. M., Navas, F. E., Vázquez-López-Escobar, A., & Mejías, M. B. (2006). Tidal induced variability of mixing processes on Camarinal Sill (Strait of Gibraltar): A pulsating event. *Journal of Marine Systems*, 60(1–2), 177–192. <https://doi.org/10.1016/j.jmarsys.2005.12.003>
- McMillan, J. M., Hay, A. E., Lueck, R. G., & Wolk, F. (2016). Rates of dissipation of turbulent kinetic energy in a high Reynolds number tidal channel. *Journal of Atmospheric and Oceanic Technology*, 33(4), 817–837. <https://doi.org/10.1175/jtech-d-15-0167.1>
- Millot, C. (2009). Another description of the Mediterranean Sea outflow. *Progress in Oceanography*, 82(2), 101–124. <https://doi.org/10.1016/j.pocean.2009.04.016>
- Millot, C. (2014). Heterogeneities of in- and out-flows in the Mediterranean Sea. *Progress in Oceanography*, 120, 254–278. <https://doi.org/10.1016/j.pocean.2013.09.007>
- Millot, C. (2017). Definitive evidence of the Mediterranean Outflow heterogeneity. Part 2: All along the Strait of Gibraltar. *Ocean Science*, 53.
- Moum, J. (1996). Energy-containing scales of turbulence in the ocean thermocline. *Journal of Geophysical Research*, 101(C6), 14095–14109. <https://doi.org/10.1029/96jc00507>
- Naranjo, C., García-Lafuente, J., Sammartino, S., Sánchez-Garrido, J. C., Sánchez-Leal, R., & Jesús Bellanco, M. (2017). Recent changes (2004–2016) of temperature and salinity in the Mediterranean Outflow. *Geophysical Research Letters*, 44(11), 5665–5672. <https://doi.org/10.1002/2017GL072615>
- Naranjo, C., García-Lafuente, J., Sannino, G., & Sanchez-Garrido, J. (2014). How much do tides affect the circulation of the Mediterranean Sea? From local processes in the Strait of Gibraltar to basin-scale effects. *Progress in Oceanography*, 127, 108–116. <https://doi.org/10.1016/j.pocean.2014.06.005>
- Naranjo, C., Sammartino, S., García-Lafuente, J., Bellanco, M. J., & Taupier-Letage, I. (2015). Mediterranean waters along and across the Strait of Gibraltar, characterization and zonal modification. *Deep-Sea Research I*, 105, 41–52. <https://doi.org/10.1016/j.dsr.2015.08.003>
- Nash, J. D., Peters, H., Kelly, S. M., Pelegrí, J. L., Emelianov, M., & Gasser, M. (2012). Turbulence and high-frequency variability in a deep gravity current outflow. *Geophysical Research Letters*, 39(18). <https://doi.org/10.1029/2012GL052899>
- Osborn, T. (1980). Estimates of the local rate of vertical diffusion from dissipation measurements. *Journal of Physical Oceanography*, 10(1), 83–89. [https://doi.org/10.1175/1520-0485\(1980\)010<0083:eotfro>2.0.co;2](https://doi.org/10.1175/1520-0485(1980)010<0083:eotfro>2.0.co;2)
- Papadakis, M. P., Chassignet, E. P., & Hallberg, R. W. (2003). Numerical simulations of the Mediterranean Sea outflow: Impact of the entrainment parameterization in an isopycnal coordinate ocean model. *Ocean Modelling*, 5(4), 325–356. [https://doi.org/10.1016/S1463-5003\(02\)00042-2](https://doi.org/10.1016/S1463-5003(02)00042-2)
- Perot, J. B., & Gadebusch, J. (2009). A stress transport equation model for simulating turbulence at any mesh resolution. *Theoretical and Computational Fluid Dynamics*, 23(4), 271–286. <https://doi.org/10.1007/s00162-009-0113-x>
- Pratt, L. J., & Whitehead, J. A. (2008). *Rotating hydraulic*. Springer.
- Purwandana, A., Cuypers, Y., & Bouruet-Aubertot, P. (2021). Observation of internal tides, nonlinear waves and mixing in the Lombok Strait, Indonesia. *Continental Shelf Research*, 216(10435), 104358. <https://doi.org/10.1016/j.csr.2021.104358>
- Roustan, J.-B., Bordoïs, L., Dumas, F., Auclair, F., & Carton, X. (2023). In situ observation of the small-scale dynamics near Camarinal Sill – Strait of Gibraltar. *Journal of Geophysical Research: Oceans*, 128(10). <https://doi.org/10.1029/2023jc019738>
- Sánchez-Garrido, J., Sannino, G., Liberti, L., García Lafuente, J., & Pratt, L. (2011). Numerical modeling of three-dimensional stratified tidal flow over Camarinal Sill, Strait of Gibraltar. *Journal of Geophysical Research*, 116(C12), C12026. <https://doi.org/10.1029/2011jc007093>

- Sanchez-Roman, A., Jorda, G., Sannino, G., & Gomis, D. (2018). Modelling study of transformations of the exchange flows along the Strait of Gibraltar. *Ocean Science*, 14(6), 1547–1566. <https://doi.org/10.5194/os-14-1547-2018>
- Sannino, G., Carillo, A., & Artale, V. (2007). Three-layer view of transports and hydraulics in the Strait of Gibraltar: A three-dimensional model study. *Journal of Geophysical Research*, 112(C3). <https://doi.org/10.1029/2006JC003717>
- Sannino, G., Carillo, A., Pisacane, G., & Naranjo, C. (2015). On the relevance of tidal forcing in modelling the Mediterranean thermohaline circulation. *Progress in Oceanography*, 134, 304–329. <https://doi.org/10.1016/j.pocean.2015.03.002>
- Staalström, A., Arneborg, L., Liljebladh, B., & Broström, G. (2015). Observations of turbulence caused by a combination of tides and mean baroclinic flow over a fjord sill. *Journal of Physical Oceanography*, 45(2), 355–368. <https://doi.org/10.1175/JPO-D-13-0200.1>
- Stommel, H., & Farmer, D. (1952). Abrupt change in width in two-layer open channel flow. *Journal of Marine Research*, 11(2), 205–215.
- Stommel, H., & Farmer, D. (1953). Control of salinity in an estuary by a transition. *Journal of Marine Research*, 12(1), 13–22.
- Thorpe, S. A., & Deacon, G. E. R. (1977). Turbulence and mixing in a Scottish Loch. *Philosophical Transactions of the Royal Society of London - Series A: Mathematical and Physical Sciences*, 286(1334), 125–181. <https://doi.org/10.1098/rsta.1977.0112>
- Vargas, J., Lafuente, J. G., Candela, J., & Sánchez, A. J. (2006). Fortnightly and monthly variability of the exchange through the Strait of Gibraltar. *Progress in Oceanography*, 70(2–4), 466–485. <https://doi.org/10.1016/j.pocean.2006.07.001>
- Vladoiu, A., Bouruet-Aubertot, P., Cuypers, Y., Ferron, B., Schroeder, K., Borghini, M., et al. (2018). Turbulence in the Sicily Channel from microstructure measurements. *Deep-Sea Research Part I*, 137, 97–112. <https://doi.org/10.1016/j.dsr.2018.05.006>
- Wesson, J. C., & Gregg, M. (1994). Mixing at Camarinal Sill in the Strait of Gibraltar. *Journal of Geophysical Research*, 99(C5), 9847–9878. <https://doi.org/10.1029/94jc00256>